Research Square

Preprints are preliminary reports that have not undergone peer review.
They should not be considered conclusive, used to inform clinical practice,
or referenced by the media as validated information.

Concerted mass transport governs anomalous diffusion in anharmonic bcc metals

Davide G. Sangiovanni

davide.sangiovanni@liu.se

Linköping University

Carlos R. Salazar

Linköping University

Ferenc Tasnádi

Linköping University

Johan Klarbring

Linköping University

Igor A. Abrikosov

Linköping University

Article

Keywords:

Posted Date: April 2nd, 2026

DOI: https://doi.org/10.21203/rs.3.rs-9179563/v1

License: This work is licensed under a Creative Commons Attribution 4.0 International License.
Read Full License

Additional Declarations: No competing interests reported.

Concerted mass transport governs anomalous diffusion in anharmonic bcc metals

Davide G. Sangiovanni,[1*] Carlos R. Salazar,[1] Ferenc Tasnádi,[1] Johan Klarbring,[1]
Igor A. Abrikosov[1]

[1]Department of Physics, Chemistry, and Biology (IFM) Linköping University, SE-581 83, Linköping, Sweden

Understanding the microscopic origin of anomalous self-diffusion near melting remains a central challenge in bcc metals. Here we combine *ab initio* and machine-learning interatomic-potential molecular dynamics simulations (AIMD, MLIP-MD) to elucidate the mechanisms governing high-temperature mass transport in group-3–6 metals. Comparative AIMD simulations near melting reveal a clear distinction between dynamically-stabilized group-3 and group-4 bcc metals and the quasiharmonic group-5 and group-6. In the former, characterized by strongly anharmonic energy landscapes, sufficiently large thermal displacements of individual atoms trigger cascades of cooperative transport, including ring exchanges and spontaneous formation and migration of vacancy–crowdion-like Frenkel pairs. In contrast, diffusion in quasiharmonic bcc metals remains dominated by conventional vacancy-mediated mechanisms. Temperature-dependent MLIP-MD simulations of bcc Ti, taken as a representative dynamically-stabilized system, further show that migration rates of isolated point defects remain Arrhenius-like upon cooling toward dynamical instability. The curvature in self-diffusivity near melting instead originates from thermally activated collective reactions within nominally pristine lattice regions. Structural analysis reveals transient ω-like local environments as fingerprints of lattice softening accompanying these correlated dynamics. Together, these results identify anharmonic energy landscapes as the origin of anomalous diffusion in dynamically-stabilized bcc metals and suggest a general framework for high-temperature transport in crystalline solids.

*Corresponding author: davide.sangiovanni@liu.se

1. Introduction

Mass transport governs structural evolution, phase stability, phase transformations, and mechanical response in crystalline materials. In elemental solids, diffusion is traditionally described as migration of intrinsic point defects – lattice vacancies and self-interstitial atoms – which form at surfaces, extended structural defects, or via spontaneous Frenkel-pair generation within the bulk. In the dilute-defect limit, transport is commonly modeled as stochastic hopping between equivalent lattice sites. Self-interstitial atoms can, however, adopt crowdion configurations that migrate quasi-one-dimensionally along close-packed directions through synchronous displacements of neighboring atoms driven by the local compressive field introduced by the excess atom [1, 2]. Vacancies may likewise form small clusters that migrate faster than isolated vacancies through one-dimensional collective rearrangements (voidions) [3, 4]. In both cases, mass transport remains mediated by native point defects. Recent atomistic studies, however, indicate that concerted atomic migration – involving atomic ring exchanges or correlated motion of transient vacancy–interstitial configurations emerging in nominally defect-free regions – can provide an additional diffusion channel in elemental crystals.

Early theoretical work already suggested the possibility of correlated atomic dynamics, including direct neighbor interchange and cooperative atomic-ring rotations, as alternative pathways to conventional defect-mediated diffusion in metals like Cu [5, 6] and covalent solids such as Si [7]. More recently, molecular dynamics simulations have provided atomistic evidence that collective migration processes can significantly influence mass transport and structural properties in monoatomic crystals. In many systems, activation of these processes occurs under extreme thermodynamic conditions, for example under inner-core pressures and temperatures in Fe [8-10], in compressed phases of Ca [11] and Li [12] and in complex host–guest structures emerging in K at high pressure and near melting [13]. Only a limited number of studies have reported concerted diffusion at ambient pressures. Classical molecular dynamics (CMD) simulations provided the first direct observation in high-temperature bcc Zr [14]. Our recent work demonstrated picosecond-scale collective diffusion reactions in bcc Ti near melting, involving frequent spontaneous Frenkel-pair formation, migration, and recombination together with ring-exchange events [15]. We further proposed that these processes contribute to the well-known non-Arrhenius temperature dependence of self-diffusion in dynamically-stabilized bcc metals [16, 17]. Subsequent simulations based on semi-empirical and machine-learning interatomic potentials showed that similar concerted diffusion reactions emerge at lower homologous temperatures in group-4 elements than in group-5 and group-6 metals [18, 19]. Correlated atomic motion has also been implicated in martensitic transformations, diffusion, and melting in both elemental crystals and complex multicomponent alloys [20-23].

Despite these advances, the general relevance of concerted transport mechanisms in metals approaching melting remains unclear. Reported trends are sometimes contradictory, partly owing to

differing reliability of interaction models employed in classical simulations. In particular, the extent to which collective processes such as ring exchanges or transient Frenkel-pair reactions govern curvature in self-diffusivity near melting is still debated [24]. Moreover, most previous atomistic studies [15, 18, 19, 25-33] have focused on refractory systems, whereas diffusion in dynamically stabilized high-temperature bcc phases of group-3 metals such as Sc and La has received comparatively little attention.

Anomalous diffusivities in group-4 elements have long been attributed in phenomenological models to soft vibrational modes and strong lattice anharmonicity [34, 35], although these models primarily emphasized enhancement of monovacancy-mediated transport. In the present work, we combine ab initio molecular-dynamics (AIMD) and machine-learning interatomic-potential molecular-dynamics (MLIP-MD) simulations to establish systematic trends in diffusion mechanisms across group-3–6 transition metals at elevated temperatures. Our results demonstrate the widespread importance of concerted migration processes in strongly anharmonic bcc metals and reveal clear differences in diffusion pathways, transient local structural transformations, and mass-transport behavior along the periodic-table from group-3 to group-6 elements. These trends can be rationalized in terms of the underlying energy landscape and the role of soft vibrational modes of the bcc lattice, whose implications for microscopic transport have so far remained largely unresolved. In particular, the bcc phases of group-3 metals (Sc [36], Y [37, 38], and La [39-41]) and group-4 metals (Ti [42], Zr [43], Hf [44], Ce [41, 45, 46], and Th [40]) are stabilized at elevated temperature by anharmonic lattice vibrations but become dynamically unstable near ambient conditions due to phonon softening [40, 47-50], whereas group-5 and group-6 metals retain the bcc structure from 0 K up to melting [51].

2. Results and discussion

2.1. Distinct self-diffusion behavior in group-3,4 vs group-5,6 metals

AIMD simulations in the NVT ensemble were performed for six bcc metals from Groups 3–6 at homologous temperatures of approximately 0.93 T_m^{expt}, where T_m^{expt} denotes the experimental melting temperature. Equilibrium lattice parameters, obtained from prior NpT equilibration, are in close agreement with reported experimental values (**Table 1**). **Figure 1** presents superpositions of atomic configurations over 25 ps, with each configuration averaged over 1 ps to suppress vibrational noise and enhance the visibility of migration mechanisms; atoms are colored according to simulation time to illustrate their temporal evolution. In group-5 vanadium and group-6 molybdenum (**Fig. 1e,f**), all atoms remain close to their ideal bcc positions throughout the simulation, consistent with the stability of the bcc phase in these metals from 0 K to melting. In contrast, dynamically stabilized and strongly anharmonic bcc Sc and the group-4 metals exhibit concerted migration events, characterized by quasi-synchronous translations of several atoms between lattice sites (**Fig. 1a–d**). The persistence

of near-ideal average atomic positions and the fluctuation of the DFT stresses σ_{xx}, σ_{yy}, and σ_{zz} around zero indicate that the systems do not undergo melting (as exemplified for bcc Ti in **Fig. S2** of the **Supplemental Material** (**SM**)). Nevertheless, since PBE-based DFT calculations typically underestimate melting temperatures by 2–10% [52-54], the possibility that some simulations probe overheated states cannot be fully excluded. AIMD **Supplementary Videos** of bcc Sc (**Video 1**), Ti (**Video 2**), Zr (**Video 3**), Hf (**Video 4**), and V (**Video 5**) are provided in the **SM** (see also **Sec. S6**). A corresponding video for bcc Mo is not included because no atomic migration events are observed within the simulated time, similarly to the case of bcc V.

Concerted migration in dynamically stabilized bcc phases initiates when a sufficiently large atomic displacement triggers correlated motion of neighboring atoms. Such perturbations can propagate as rapid (ps-scale) atomic-ring rotations or through the formation of vacancy-self-interstitial pairs that subsequently migrate independently. In the following, we rationalize the competition between individual atomic jumps and collective displacements in terms of the underlying potential energy landscape. Most chains observed in Sc, Ti, Zr, and Hf propagate along ⟨111⟩ directions, although **Fig. 1a–d** also reveals collective translations parallel to ⟨001⟩ axes. This is consistent with experimental studies on bcc Ti [55], which reported that while diffusion predominantly follows ⟨111⟩ nearest-neighbor paths, approximately 10–15% of events occur along next-nearest-neighbor ⟨001⟩ directions. Notably, Ref. [55] attributed diffusion exclusively to single- and di-vacancy jumps, without considering other mechanisms.

Figure 1 illustrates qualitatively different behaviors in group-3,4 vs group-5,6 crystals. The activation of concerted migration – mediated by Frenkel-pair formation and subsequent point-defect diffusion or ultrafast (~ps) atomic-ring rotation – yields non-zero self-diffusion coefficients in Sc and group-4 metals even though the supercell models are initialized without point defects. **Table 1** reports the self-diffusivities (D^{AIMD}) computed during 25 ps by linear fitting of mean-squared displacements vs time. The AIMD and experimental (D^{expt}) results of self-diffusion coefficients in bcc group-4 metals at $T_{\mathrm{sim}} \approx 0.93–0.94\ T_{\mathrm{m}}^{\mathrm{expt}}$ are

- Titanium: $D^{\mathrm{AIMD}}=(5.3\pm0.4)\cdot10^{-11}$ m$^2\cdot$s^{-1}; $D^{\mathrm{expt}}\approx(0.8–1)\cdot10^{-11}$ m$^2\cdot$s^{-1} [16, 17, 55-57],
- Zirconium: $D^{\mathrm{AIMD}}=(10.6\pm0.5)\cdot10^{-11}$ m$^2\cdot$s^{-1}; $D^{\mathrm{expt}}\approx(1–4)\cdot10^{-11}$ m$^2\cdot$s^{-1} [34, 58, 59],
- Hafnium: $D^{\mathrm{AIMD}}=(6.0\pm0.6)\cdot10^{-11}$ m$^2\cdot$s^{-1}; $D^{\mathrm{expt}}\approx(2–4)\cdot10^{-11}$ m$^2\cdot$s^{-1} [57, 60].

The systematic overestimation in AIMD primarily reflects (i) the known 2–10% underestimation of melting temperatures within DFT/PBE [52-54], effectively placing the simulations closer to melting, and (*ii*) periodic boundary conditions in defect-free cells that impose equal concentrations of vacancies and self-interstitials. Because self-interstitials are more mobile, this artificial balance inflates diffusion coefficients. Notably, the self-diffusion coefficient obtained for bcc Sc at T ~0.92 $T_{\mathrm{m}}^{\mathrm{expt}}$, $D^{\mathrm{AIMD}}=(37.5\pm1.5)\cdot10^{-11}$ m$^2\cdot$s^{-1}, is between four and seven times larger than in Ti, Zr, and Hf.

This underscores that the anomalously high premelting self-diffusivities of bcc metals are most pronounced in group-3 systems.

The AIMD results in **Fig. 1** highlight the role of anharmonic lattice vibrations in governing the anomalous mass transport of group-3 and group-4 bcc metals. The influence of soft phonon modes in facilitating atomic migration in group-4 bcc systems has been discussed previously (e.g., Refs. [18, 31, 32, 35, 43, 61]). In particular, neutron-scattering experiments show that bcc Sc [36], La [39], Ti [42], Zr [43], and Hf [44] exhibit strongly damped longitudinal 2/3[111] (ω) modes, whose frequencies decrease with decreasing *d*-electron count (see figure 7 in Ref. [62]). First-principles analyses further indicate that rigid displacements of ⟨111⟩ atomic rows induce electron localization within the row and concomitant screening of inter-row interactions, thereby reducing resistance to shear along ⟨111⟩ directions [63]. Importantly, the resulting anomalously high self-diffusivities are not restricted to the high-temperature bcc phase. A weakly corrugated potential energy surface [64] with comparatively low migration barriers [65] characterizes both hcp and bcc structures, as confirmed by MLIP-MD simulations of group-4 metals [19]. More generally, similar diffusion anomalies may be expected in Y [37, 38], La [39-41], Ce [41, 45, 46], and Th [40], consistent with the shared lattice anharmonicity and related phase behavior of group-3 and group-4 metals.

The facile activation of concerted migration mechanisms in dynamically-stabilized bcc metals is rationalized from the results of static DFT calculations obtained for Sc, Ti, V, and Mo in **Fig. 2**. **Figure 2a** represents the energy variation due to a [111] displacement of a lattice atom (blue) when the preceding neighbor along the chain (red) is fixed at a distance $\boldsymbol{r}_2$ from the ideal bcc position. Conversely, **Fig. 2b** shows the energy change upon [111] translation of the red atom while the following blue atom is held at a prescribed displacement $\boldsymbol{r}_1$ from its original lattice site. Both panels are derived from the same DFT dataset and emphasize complementary aspects of the local energy landscape. The results reveal that in Sc and Ti the ideal bcc position becomes unstable when the preceding (**Fig. 2a**) or following (**Fig. 2b**) atom is displaced by approximately 0.15 d_{NN}, where d_{NN} denotes the nearest-neighbor distance. In contrast, atoms in bcc V and Mo remain in a quasi-harmonic energy landscape even when their nearest neighbors are substantially displaced from their lattice sites. This behavior, associated with the soft ω phonon mode of the bcc phase, reflects the incipient dynamical instability of the lattice at lower temperatures [31, 32, 74, 75]. The strongly anharmonic energy landscape of bcc Sc and Ti therefore generates a pull–push interaction between neighboring atoms when one atom is displaced along a ⟨111⟩ direction. Consequently, native vacancies and self-interstitials are expected to locally amplify the intrinsic pull–push instability along ⟨111⟩ chains, thereby promoting correlated migration events, although such collective motion is already inherent to the anharmonic lattice even in the absence of defects.

2.2. Mass transport mechanisms in a dynamically-stabilized lattice: bcc Ti

We perform machine-learning interatomic potential molecular dynamics (MLIP-MD) simulations to investigate temperature-dependent mass-transport mechanisms in bcc Ti, chosen as a prototypical dynamically stabilized phase. Experimentally, the bcc phase is thermodynamically stable between 1155 K and the melting temperature ($T_m^{expt} \approx 1940$ K) at ambient pressure, but unstable at 0 K [50]. Our MLIP-MD simulations in the NpT ensemble indicate that the bcc structure becomes metastable above ≈650 K, whereas at lower temperatures it transforms rapidly (within a few picoseconds) to the hcp phase (see **Sec. 2.3**). The temperature dependence of equilibrium lattice parameters for bcc supercells, with and without point defects, is shown in **Fig. S1**. As expected, self-interstitials lead to a slight lattice expansion, while vacancies cause lattice contraction.

MLIP-MD simulations between $650 \leq T \leq 1900$ K yield Ti self-diffusion coefficients $D(T)$ for initially defect-free as well as defective (monovacancy or self-interstitial) bcc supercells (**Fig. 3**), extracted from atomic trajectories using **Eq. 1** (see Methods in **Sec. 4.2**). At all temperatures, self-interstitials diffuse only about 1.5–2.5 times faster than vacancies, in contrast to their typically much higher mobility in metals [66, 67] and ceramics [68]. In either case, migration proceeds in a highly correlated manner, even at relatively low temperatures. For example, simulations at 900 K show vacancy motion occurring via concerted rotation of a five-atom string within the (011) plane (**Fig. S3**), whereas self-interstitial transport occurs through synchronous displacements of extended ⟨111⟩ atomic chains (**Fig. S4**), corresponding to fast crowdion-type diffusion driven by compressive strain in close-packed rows [1, 2]. The degree of crowdion character evolves dynamically during migration, being most pronounced during propagation along a given ⟨111⟩ direction and decreasing when the defect trajectory curves toward another propagation path; for clarity, such configurations are therefore referred to here as *crowdion-like*. Relaxation of atoms toward a vacancy generates a local tensile distortion (**Fig. S5**), while crowdion-type self-interstitials impose compressive strain along close-packed rows. These defect-induced lattice distortions, reflecting the strong anharmonicity of bcc Ti (**Fig. 2**), promote concerted migration in which displacements of neighboring atoms occur nearly simultaneously.

At elevated temperatures, the correlated dynamics described above emerge spontaneously within initially defect-free regions. As illustrated in **Fig. 4** for bcc Ti at 1400 K, a sufficiently large thermal displacement of a lattice atom can produce a vacancy–crowdion-like Frenkel pair. The lattice distortion associated with self-interstitial formation promotes cooperative ⟨111⟩ displacement of neighboring atoms (shown in red in **Fig. 4c,d**), while the vacancy left behind (empty red circle in **Fig. 4g,h**) attracts nearby atoms (shown in yellow). The Frenkel pair may subsequently separate and migrate independently or remain dynamically coupled. In the latter case, correlated motion of the vacancy and crowdion-like defect closes into a cyclic exchange pathway. **Figure 5** shows an example

of such event – a ten-atom ring rotation at 1400 K – in which atoms are transported through coordinated substitutions while local neighbor connectivity is preserved. During this process, atoms adjacent to the transiently vacated site relax out of their positions, analogous to the vacancy-induced relaxation shown in **Fig. S5**. The event may thus be interpreted as a short-lived Frenkel pair migrating in opposite directions along the ring before recombining and annihilating. If recombination does not occur, the chain breaks, producing spatially separated vacancy and crowdion-like defects. The atomistic reaction pathways illustrated in **Figs. 4 and 5** are consistent with mechanisms predicted in earlier CMD simulations of bcc Ti [18].

More generally, diffusion in bcc Ti proceeds through concerted atomic motion irrespective of whether it is initiated by an isolated vacancy, a self-interstitial, a spontaneously formed Frenkel pair, or a ring exchange reaction. MLIP-MD simulations also reveal that vacancies and crowdion-like interstitials interact through long-range lattice distortions, giving rise to *bridge reactions*. An example is shown in **Fig. 6**, where a vacancy (green arrow) and a self-interstitial (ring of five orange atoms), initially separated by ~1.5 nm, become abruptly connected by a straight ⟨111⟩ atomic chain (red spheres), enabling rapid recombination and restoration of a defect-free lattice. Such long-range defect coupling blurs the distinction between Frenkel-pair formation followed by migration and direct ring-exchange events. In particular, cooperative recombination of two nearby Frenkel pairs formed quasi-simultaneously can generate atomic displacement patterns essentially indistinguishable from large ring exchanges. The apparent mechanistic difference therefore depends primarily on whether transient vacancy–interstitial configurations are resolved on timescales comparable to the exchange process, rendering the two descriptions largely equivalent manifestations of the same collective transport phenomenon.

2.3. Trends in self-diffusivities near dynamical instabilities

MLIP-MD simulations allow us to gain statistical confidence on self-diffusivities in bcc Ti down to ~650 K. Below this temperature, NpT sampling indicates a collapse of the bcc lattice into the hcp allotrope [≈90% hcp from Steinhardt parameters (see **Sec. S5** of the **SM**)], consistent with the onset of dynamical instability. Earlier AIMD and CMD results likewise place the metastability limit of bcc Ti between ~650–750 K, with transformation into ω or hcp depending on boundary conditions [69, 70].

Between 650 and 1000 K, the self-diffusion coefficients of vacancy- and self-interstitial–containing bcc Ti supercells follow Arrhenius behavior: $D^{V}(T) = [(3.0\pm1.3)\cdot10^{-8}\ m^2s^{-1}]\cdot\exp[(-0.13\pm0.03\ eV)/(k_BT)]$ and $D^{SI}(T) = [(7.8\pm2.8)\cdot10^{-8}\ m^2\ s^{-1}\cdot\exp[(-0.14\pm0.03\ eV)/(k_BT)]$ (red and blue lines in **Fig. 3**). The persistence of Arrhenius trends upon cooling to 650 K is unexpected given the proximity to phonon instabilities, where substantial modifications of the free-energy landscape might be anticipated. As discussed in Ref. [71], competing effects can rationalize this behavior: phonon

softening reduces both the migration barrier E_m and the curvature of the effective potential (U_{eff}) at the equilibrium position r_{eq}, thereby lowering the attempt frequency $\nu \propto \sqrt{|\partial^2 U_{eff}/\partial r^2|_{r=r_{eq}}}$ [72]. Simultaneous reductions in ν and E_m compensate in the migration rate $\Gamma(T) = \nu(T)\cdot\exp[-E_m(T)/(k_B T)]$, preserving a linear log(D) vs $1/T$ dependence (neglecting defect concentrations). This finding reframes earlier interpretations of diffusion anomalies in group-4 metals. Previous studies attributed curvature in log(D) vs $1/T$ to the incipient bcc → ω transformation upon cooling [34]. Instead, **Fig. 3** shows that migration rates remain Arrhenius-like below ~1100 K. Any experimental bowing upon cooling toward the bcc → hcp transition must therefore arise from non-Arrhenius temperature dependence of equilibrium defect concentrations, reflecting changes in vacancy formation free energy [19, 73]. In contrast, the curvature observed upon heating originates from thermally activated diffusion events in nominally defect-free regions.

2.4. Diffusion in nominally defect-free regions and the breakdown of Arrhenius behavior

Deviations from Arrhenius behavior in self-diffusivities are observed in essentially all refractory metals near melting. In group-6 bcc metals such as Mo and W, these deviations can largely be rationalized by temperature-dependent modifications of vacancy migration barriers and/or non-Arrhenius equilibrium vacancy concentrations within an otherwise monovacancy-dominated diffusion mechanism [25, 27-29, 33]. In dynamically stabilized bcc metals, however, the origin is fundamentally different. Using bcc Ti as a representative system, we show that the self-diffusion anomalies of group-4 metals originate from spontaneous nucleation of vacancy–crowdion-like Frenkel-pairs and ring-exchange events in an initially pristine lattice. Atomistic simulations that explicitly capture these reactions quantitatively reproduce the experimentally observed curvature of the diffusivity near melting.

To enable comparison between MLIP-MD diffusivities and experimental measurements, equilibrium point-defect concentrations must be established. These are evaluated by annealing large surface-slab models at elevated temperature using MLIP-MD simulations (see **Sec. S3** of the **SM**). As a reference, we first examine bcc tungsten, in which point defects remain dilute and spontaneous Frenkel-pair formation is not observed within the accessible simulation times. Diffusion in W is therefore largely governed by monovacancy migration and exhibits only weak deviations from Arrhenius behavior near melting [25]. We then describe the more complex defect dynamics characteristic of bcc Ti.

A bcc W(001) surface slab – initialized with vacancies to accelerate convergence – is annealed at 3000 K using the MLIP of Ref. [25], see **Fig. S6f** in **SM**. Because the potential was trained on DFT/PBE data, we assume that the corresponding DFT/PBE estimate of the melting temperature (T_m = 3349 K [52]) also applies to the MLIP description. For sufficiently large systems, the slab geometry

does not influence the equilibrium concentration of point defects [74]. Under these conditions tungsten exhibits a dilute population of vacancies that remain well localized on lattice sites and migrate in essentially uncorrelated manner even at $T \approx 0.9\,T_m$, consistent with the conventional diffusion picture illustrated in **Fig. 7a**. No self-interstitial formation is detected within the simulated time window. The vacancy concentration in the slab interior fluctuates weakly around $c_V=(7.1\pm3.0)\times10^{-5}$, in good agreement with $[(8.3\pm1.3)\times10^{-5}]$ predicted from **Eq. 4** using $G^f_V(3000\text{ K}) = 2.43\pm0.04$ eV [25].

Having established tungsten as a benchmark exhibiting vacancy-dominated diffusion, we now turn to bcc Ti, where the Arrhenius description breaks down. MLIP-MD simulations of Ti(001) surface slabs yield a melting temperature $T_m^{MLIP} \approx 1725\pm25$ K (**Sec. S3** and **Fig. S6**), about 11% below experiment, consistent with the known tendency of DFT/PBE-based models to underestimate melting points [52-54]. Surface-slab annealing simulations are subsequently performed between 1200 K and 1700 K to determine equilibrium defect concentrations. For the analysis, it is convenient to partition the total vacancy concentration c_V (fraction of empty lattice sites) into a contribution from effectively missing atoms, c_V^{MA} (primarily surface-generated vacancies that have diffused into the slab interior), and vacancies nucleated within originally defect-free lattice regions, c_V^{DF}, which equal the concentration of self-interstitials c_{SI}^{DF} (bulk-generated Frenkel pairs). Frenkel-pair formation does not alter the net atom deficit (c_V^{MA}) in the crystal but redistributes atoms between lattice and interstitial configurations. The equilibrium concentration of missing atoms is obtained from $c_V^{MA} = 1 - (n_{atoms} / n_{sites})$. Slab models containing either 100800 or 450000 atoms are employed to assess finite-size convergence. Agreement of $c_V^{MA}(T)$ values at 1300 K and 1500 K (**Table 2**) confirms convergence within statistical uncertainty. Reliable equilibrium concentrations are obtained for the larger slabs at $T < 1600$ K; at higher temperature occasional force singularities in the MLIP terminate simulations prematurely, and results from smaller slabs are therefore used.

Vacancy–adatom pair formation at the Ti(001) surface and subsequent vacancy migration establish within ≈1.5 ns a steady-state defect population throughout the slab (**Fig. S7**). At 1200 K, Frenkel-pair formation and ring-exchange events remain relatively rare, so diffusion is dominated by migration of surface-generated vacancies. With increasing temperature, however, spontaneous nucleation of Frenkel defects and collective atomic rearrangements in initially defect-free regions becomes progressively more frequent. These transient vacancy–crowdion-like pairs fluctuate strongly on picosecond time scales owing to dissociation, recombination, and interactions with other defects (see **Fig. 7b**). The equilibrium concentrations of missing atoms determined from Ti(001) annealing are summarized in **Table 2** together with the mean atom-deficit concentration $\langle c_V^{TI}(T)\rangle$ predicted by the dilute-limit relation (**Eqs. 3, 4**) using vacancy-formation free energies $G^f_V(T)$ calculated via

thermodynamic integration in Ref. [19]. We find that the $\langle c_V^{TI}(T)\rangle$ values systematically exceed the slab-derived concentrations $c_V^{MA}(T)$. This difference is likely due to the distinct thermodynamic and kinetic constraints inherent to the two approaches. The dilute-limit expression corresponds to equilibrium with an ideal atomic reservoir and neglects defect–defect correlations, whereas the surface-slab simulations explicitly capture the coupled processes of surface emission, bulk diffusion, and recombination that determine the steady-state atom deficit in the finite system. The slab-derived concentrations therefore represent a direct atomistic measure of the effective equilibrium missing-atom population.

Although Frenkel-pair formation and ring-exchange reactions do not modify c_V^{MA}, their increasing activity in bcc Ti at elevated temperature contributes directly to atomic transport and underlies the breakdown of Arrhenius behavior. To quantify this effect, we perform independent MLIP-MD simulations between 1200 K and 1700 K in fully periodic 27×27×27 bcc supercells (~40000 atoms) initialized with vacancy concentrations chosen to match the equilibrium $c_V^{MA}(T)$ values obtained from surface-slab annealing (**Table 2**). The resulting diffusivities (extracted from atomic mean-squared displacements, **Eq. 1**, **Sec. 4.2**) therefore include contributions from both migration of permanent vacancies (*i.e.*, c_V^{MA}) and diffusion processes activated in nominally pristine lattice regions, including atomic ring rotations and spontaneous vacancy–crowdion-pair reactions. To approximate the contribution of permanent vacancies alone, we construct a vacancy-only reference by multiplying $c_V^{MA}(T)$ values with the concentration-independent monovacancy diffusivity $D^V_{c\text{-indep.}}(T) = D_0^V \exp[-E_m^V/(k_B T)]$, where $E_m{}^V$ = 0.13±0.03 eV and $D_0{}^V$ = (3.0±1.3)·10^{-8} m^2 s^{-1} are obtained from Arrhenius regression of isolated-vacancy migration frequencies at T < 1200 K (**Fig. 3**). In this regime, diffusion proceeds exclusively via monovacancy migration over the simulated time and lengthscales.

Figure 8 compares diffusivities obtained from direct MLIP-MD simulations (red pentagons), the vacancy-only reference (orange diamonds), and experimental measurements (black symbols). Because the equilibrium missing-atom concentration $c_V^{MS}(T)$ itself exhibits non-Arrhenius temperature dependence, the vacancy-only baseline also displays curvature in log(D) vs 1/T, yet remains generally below experimental values (**Fig. 8**). At 1200 K, the results of direct MLIP-MD simulations coincide with vacancy-only diffusivities, confirming vacancy-dominated transport at lower temperatures. At higher temperatures the results of direct simulations progressively exceed the vacancy-only baseline, reflecting the increasing contribution of diffusion processes activated in initially defect-free regions of the lattice. Only the full MLIP-MD simulations reproduce the experimentally observed curvature of the diffusivity near melting, demonstrating the emergence of an additional non-Arrhenius transport channel associated with spontaneous Frenkel-pair formation

and collective atomic rearrangements. As melting is approached, cooperative defect–defect interactions such as the bridge reactions illustrated in **Fig. 6** become increasingly frequent and further enhance atomic mobility.

2.5. Connection between anomalous diffusion and ω structure

Previous studies have proposed that the anomalous temperature dependence of self-diffusion in group-4 bcc metals is associated with the transient formation of hexagonal ω-structure embryos [34]. In these models, the curvature observed in Arrhenius plots of the self-diffusion coefficient was interpreted as arising from an increasing probability (upon cooling toward the bcc → hcp transformation temperature) of forming local ω-like configurations. These motifs were proposed to facilitate vacancy migration by locally lowering migration barriers through collective atomic rearrangements.

Figure 9 provides direct atomistic evidence for the transient occurrence of ω-like environments in bcc Ti. Steinhardt analysis reveals short-lived deviations from the bcc local environment, manifested as localized ω-like motifs that form and disappear on picosecond time scales. In defect-free MLIP-MD simulations, these ω-like environments (often accompanied by a minor hcp-like contribution) occur with higher probability at elevated temperatures, while their time-averaged fraction decreases rapidly upon cooling. Throughout these simulations, the bcc lattice remains globally stable (**Fig. 9a**), and neither fcc- nor liquid-like local order is detected over nanosecond time scales. Importantly, in MLIP-MD simulations containing explicit vacancies at lower temperatures, ω-like local environments are mainly detected in the immediate vicinity of the defect. This observation indicates that, in the low-temperature regime, ω-like embryos may indeed assist vacancy migration, consistent with earlier interpretations. At the same time, the absence of ω-like environments in defect-free regions at low temperature suggests that their relevance in this regime is largely promoted by the presence of point defects. Our results therefore do not contradict the earlier ω-embryo–assisted vacancy-migration picture at low temperature. Rather, the present findings extend this interpretation to high-temperature conditions, where the time-averaged occurrence of ω-like motifs increases even in defect-free regions and coincides with the onset of concerted diffusion mechanisms, including Frenkel-pair formation and migration and atomic-ring exchanges. In this regime, ω-like environments appear as transient structural fingerprints of a softened, strongly anharmonic lattice, which enables correlated atomic motion beyond conventional vacancy hopping.

Taken together, **Figs. 8 and 9** suggest a unified picture in which ω-like local order plays distinct but interconnected roles across temperature regimes. At low temperature, ω-like embryos occur primarily near vacancies and may facilitate vacancy migration. At elevated temperature, however, similar motifs emerge more broadly as transient structural signatures of collective atomic rearrangements, which enhance self-diffusion beyond vacancy-controlled Arrhenius behavior. This

interpretation reconciles earlier phenomenological models with an atomistic description that incorporates both defect-assisted diffusion and high-temperature collective transport mechanisms. Additional support for this interpretation is provided by Steinhardt analysis of AIMD trajectories at $T \approx 0.9T_m$. As shown in **Fig. 10**, this analysis reveals a substantial and persistent population of ω-like local environments in bcc Sc and Ti, coexisting with the bcc matrix throughout the simulations. In contrast, the same analysis applied to bcc V and Mo shows a clear dominance of bcc local order, with no detectable ω-like environments in the time-averaged dynamics (consistent with no diffusion reactions in **Fig. 1**). The absence of ω embryos in V and Mo at comparable reduced temperatures demonstrates that the emergence of ω-like local order is not a generic feature of bcc metals near melting. Instead, it is characteristic of dynamically stabilized group-3 and group-4 bcc phases, where strong lattice anharmonicity promotes correlated atomic motion. These AIMD results independently substantiate the MLIP-MD findings and reinforce the conclusion that ω-like environments are signatures of lattice softening and collective dynamics in anharmonic bcc systems, rather than a universal precursor to diffusion in all bcc metals.

3. Summary and outlook

We elucidate the microscopic origin of anomalous self-diffusion in dynamically stabilized bcc metals by combining AIMD and MLIP-MD simulations over a wide temperature range. AIMD simulations at $T \approx 0.9T_m$ reveal a clear mechanistic distinction between dynamically stabilized group-3 and group-4 bcc metals and the more harmonic bcc lattices of group-5 and group-6 metals. In Sc, Ti, Zr, and Hf, diffusion occurs through highly correlated atomic rearrangements even in originally defect-free crystal models, including atomic-ring exchanges and spontaneous formation and migration of vacancy–crowdion-like defect pairs. In contrast, no diffusion events are observed in V and Mo over comparable time scales. MLIP-MD simulations of bcc Ti further demonstrate that migration rates of isolated vacancies and self-interstitials remain well described by Arrhenius behavior even upon cooling toward the temperature (~650 K) at which the bcc phase becomes dynamically unstable. We show that vacancy migration governs mass transport at $T \leq 1200$ K, whereas the curvature in self-diffusivity observed on approaching melting originates from diffusion reactions activated within nominally defect-free regions. These include Frenkel-pair formation, migration, and recombination together with atomic ring-exchange processes. Such collective reactions introduce an additional transport channel beyond conventional vacancy-controlled diffusion and give rise to strongly non-Arrhenius diffusivity trends near melting. Structural analysis reveals that concerted diffusion events are accompanied by transient ω-like local environments. At lower temperatures these motifs remain localized near vacancies and may assist vacancy migration, consistent with earlier phenomenological models. At elevated temperatures, however, ω-like

environments emerge more broadly as signatures of correlated atomic motion activated within pristine crystal domains.

More generally, the present findings illustrate how lattice anharmonicity facilitates activation of additional mass-transport mechanisms at elevated temperatures. We suggest that collective migration processes may also contribute to other lattice-instability-driven phenomena. These include, for example, nucleation of nanoscale ω embryos or precipitates in Ti-based and multicomponent alloys – where formation of a stable ω phase is often associated with embrittlement and suppression of martensitic transformations – as well as emergence of complex high-pressure phases such as host–guest structures observed in several elemental metals, and development of short-range B2-type chemical ordering reported in some bcc solid solutions at elevated temperatures. Such connections point toward a broader physical scenario in which concerted atomic migration influences diffusion kinetics, promotes local structural transformations, and affects phase stability. Clarifying the thermodynamic and structural conditions under which cooperative transport mechanisms arise in chemically complex alloys may therefore be important for advancing understanding of diffusion-controlled transformation pathways, stress-assisted phase-transformation plasticity, and stability limits in materials operating under extreme temperature or pressure conditions.

4. Computational Methods

4.1. DFT calculations and AIMD simulations

Density functional theory (DFT) and *ab initio* molecular dynamics simulations (AIMD) are carried out using VASP implemented with the projector augmented-wave method [75, 76]. Both DFT and AIMD employ Γ-point sampling of the Brillouin zone and 300 eV cutoff energies, while the electronic exchange and correlation energies are approximated by the Perdew-Burke-Ernzerhof (PBE) functional [77]. DFT calculations are used to qualitatively understand the distinct mass-transport mechanisms in quasi-harmonic group-5 and group-6 vs anharmonic group-3 and group-4 bcc metals. The supercells are free of defects and contain 1458 atoms. To study the energy landscape during migration, individual atoms are displaced along the nearest-neighbor [111] direction of the bcc lattice. A pair of nearest neighbors (named atom 1 and atom 2) was selected and the energy of the whole system was calculated after moving atom 1 closer to atom 2 in steps of 5% up to 25% of the nearest neighbor distance. The procedure is repeated after moving atom 2 further away from atom 1 in similar steps. During these calculations, all atoms are kept fixed at their designated position. This allows to assess how the energy landscape around an individual atom varies as a function of the empty space left upon displacement of the neighbor atom.

In AIMD simulations, all supercells are comprised of 9×9×9 conventional bcc cells, for a total of 1458 lattice sites. The supercell size is commensurate with the ω hexagonal phase [69]. Note that

smaller sizes could prevent activation of concerted diffusion due to limited vibrational degrees of freedom [8, 78]. AIMD simulations follow the dynamics of initially defect-free bcc Sc, Ti, Zr, Hf, V, and Mo during ~25 ps and at homologous temperatures ≈0.93 T_m. The classical equations of motion are integrated on 1-fs timesteps in the NVT ensemble using the Nose Hoover thermostat. Prior to collecting statistics, the supercells are equilibrated (residual average pressures < 200 MPa) using NPT sampling. **Table 1** lists the computed equilibrium lattice parameters and experimental melting points of the investigated systems.

4.2. MLIP-MD simulations

4.2.A. Diffusion in AIMD-size supercells. MLIP-MD simulations of bcc Ti and bcc W are based on moment-tensor potentials [79], as trained in Refs. [19] and [25]. The simulations are carried out using LAMMPS [80]. Titanium and tungsten are chosen as representative systems for dynamically-stabilized bcc metals and stable bcc phases from 0 K up to melting. 9×9×9 bcc supercells (1458 lattice sites) are first equilibrated in the NpT ensemble at a targeted temperature to determine equilibrium volumes and then used in NVT simulations to evaluate the temperature dependence of the diffusion coefficients of individual vacancy (V) and self-interstitial (SI) point defects. Additional MLIP-MD simulations of defect-free supercells (DF; all sites initially occupied) allow us to determine the self-diffusivity (D^{DF}) due to spontaneous Frenkel pair formation and migration, and ring exchange reactions. For each temperature and supercell model, we carry out 10 independent simulations, each of duration of 1 ns, using a timestep of 1 fs.

The per-atom diffusion coefficient at a given temperature is computed by

$$D = \lim_{t\to\infty} \frac{1}{\mathrm{N}} \sum_{i=1}^{N} \frac{[\boldsymbol{r}_i(t) - \boldsymbol{r}_i(t=0)]^2}{6t}, \quad \textbf{(1)}$$

where N is the number of atoms in the supercell and $\boldsymbol{r}_i(t)$ is atom's i position at time t. In this work, initially defect-free supercells contain N=1458 atoms, whereas N=1457 or 1459 for a supercell that contains one vacancy (V) or one self-interstitial (SI) defect. In practice, the diffusivity is extracted by linear regression of the mean square displacement ($\mathrm{MSD}(t) = \sum_{i=1}^{N} \frac{[\boldsymbol{r}_i(t) - \boldsymbol{r}_i(t=0)]^2}{N}$) vs time t. The error bars on the self-diffusivities represent standard deviations obtained by partitioning the full MSD-time dataset into subsets and performing fits for each subset. To evaluate the effective contribution to mass transport of an individual point defect, it is useful to introduce the concentration-independent diffusivity

$$D_{\text{c-indep.}}^{\text{V / SI}} = \lim_{t\to\infty} \sum_{i=1}^{N} \frac{[\boldsymbol{r}_i(t) - \boldsymbol{r}_i(t=0)]^2}{6t}, \quad \textbf{(2)}$$

computed by multiplying **Eq. 1** by N. If the native point defect is the only species that migrates during the simulation, the results of **Eq. 2** remain invariant with the supercell size (see **Sec. S2** of the **SM**).

4.2.B. Vacancy equilibrium concentrations. Vacancy formation free energies $G^{f}_{V}(T)$ in bcc Ti and bcc W were determined by thermodynamic integration (TI) in Refs. [19, 25] using the same MLIPs employed here. In that framework the formation free energy was defined as the free-energy change associated with removing one atom from the crystal and exchanging it with an external reservoir. The corresponding dilute-limit equilibrium concentration is therefore

$$c_{V}^{TI}(T) = \exp[-G^{f}_{V}(T)/(k_{B}T)]. \quad \textbf{(3)}$$

Assuming a normal distribution $G^{f}_{V}(T) \pm \sigma_{G}(T)$ (with $\sigma_{G}(T)$ from Refs. [19]) implies a lognormal distribution of c_{V}^{TI}. **Eq. 3** therefore yields the median concentration, whereas the experimentally relevant arithmetic mean is (see **Sec. S4** of **SM**)

$$\langle c_{V}^{TI}(T)\rangle = \exp\left(-\frac{G^{f}_{V}(T)}{k_{B}T} + \frac{\sigma_{G}^{2}(T)}{2\,(k_{B}T)^{2}}\right). \quad \textbf{(4)}$$

Because the TI formation free energy is defined through exchange of atoms with a reservoir, $\langle c_{V}^{TI}(T)\rangle$ represents the equilibrium net deficit of atoms relative to a fully occupied lattice. This quantity coincides with the total concentration of vacant lattice sites only when the population of Frenkel pairs in the bulk is negligible. We compare the equilibrium concentrations obtained from **Eq. 4** with those independently determined from high-temperature annealing of large Ti and W models with open surfaces (surface-slab approach; see **Sec. S3** of the **SM**) [27, 81, 82]. In these simulations, surface-nucleated defects diffuse into the slab interior, establishing a steady-state defect concentration throughout the material.

4.3. Structural analysis

The time-averaged statistical weights of hcp, bcc, fcc, ω, and liquid-like local atomic environments encountered along MD trajectories in nominally perfect bcc crystals are determined using Steinhardt order parameters in conjunction with Voronoi tessellation. Further methodological details are provided in **Sec. S5** of the **SM**, which also presents a scatter plot of the Steinhardt parameters for all reference structures included in the database (**Fig. S8**). Visualizations of atomic configurations and trajectories are produced using VMD [83] and Ovito [84].

Data availability

The data that support the findings of this study are available from the corresponding author upon reasonable request.

Code availability

The machine-learning interatomic potentials employed in this work were taken from previously published models (see Refs. [19,25]) and are subject to the availability conditions specified in those studies. Scripts used in the current study are available from the corresponding author upon reasonable request.

Competing interests

The authors declare no competing interests.

Author contributions

D.G.S. Conceptualization, model development, simulations, data analysis, interpretation of the results, supervision, writing-original draft, funding acquisition.

C.R.S. Simulations, data analysis, model development, interpretation of the results, writing & editing.

F.T. model development, simulations.

J.K. Interpretation of the results, scientific discussions, writing & editing.

I.A. Conceptualization, interpretation of the results, supervision, funding acquisition.

Acknowledgements

All simulations were enabled by resources provided by the National Academic Infrastructure for Supercomputing in Sweden (NAISS) at NSC in Linköping and PDC in Stockholm partially funded by the Swedish Research Council through Grant Agreements No. 2022-06725. We gratefully acknowledge Dr. Axel Forslund and Prof. Blazej Grabowski for sharing MLIPs of Ti and W. DGS and JK gratefully acknowledge financial support from the Swedish Research Council (VR) through Grants 2021-04426, 2025-04266, and 2024-05888. IAA and JK acknowledge support from the Swedish Government Strategic Research Areas in Materials Science on Functional Materials at Linköping University (Faculty Grant SFO-Mat-LiU no. 2009 00971). FT acknowledges funding support from the Swedish e-Science Research Centre (SeRC). We acknowledge support by the Knut and Alice Wallenberg Foundation (Wallenberg Scholar grant no. KAW-2023.0309).

Tables

Element	T_{sim} (K)	T_{sim}/T_m^{expt} (%)	$a(T_{sim})$ (Å)		D (during 25 ps) (10^{-11} m^2·s^{-1})
			AIMD	Experiments	
group-3					
Sc	1670	92	3.720	3.757 [85]	37.5±1.5
group-4					
Ti	1800	93	3.297	~3.34* [86]	5.3±0.4
Zr	2000	94	3.652	3.642±0.006 [87]	10.6±0.5
Hf	2350	94	3.611	~3.62 [88]	6.0±0.6
group-5					
V	2050	94	3.041	~3.09 [89]	–
group-6					
Mo	2700	93	3.215	~3.21 [89]	–

Table 1. Lattice parameters a and self-diffusion coefficients D in initially defect-free supercells of group-3–6 bcc metals at temperatures T_{sim} near experimental melting temperatures ($T_m^{expt.}$) computed via AIMD simulations during 25 ps. Diffusion is not observed in bcc V and Mo over this timeframe.
*extrapolation from experimental measurements of bcc lattice parameters between 900 and 1100 ºC.

T_{sim} (K)	T_m^{MLIP}/T_{sim}	$c_V^{MA}/10^{-4}$		$\langle c_V^{TI} \rangle /10^{-4}$
		Larger surface slab	Smaller surface slab	
bcc Ti				
1200	1.44±0.02	0.3±0.2	–	0.6±0.2
1300	1.33±0.02	0.4±0.2	0.5±0.1	1.2±0.4
1400	1.23±0.02	0.5±0.3	–	2.2±0.7
1500	1.15±0.02	1.2±0.6	1.5±0.9	3.9±1.3
1600	1.08±0.01	–	4.4±1.8	6.6±2.2
1700	1.01±0.01	–	7.4±2.5	10.9±3.9
bcc W				
3000	~1.12	–	0.7±0.3	0.83±0.13

Table 2. Equilibrium vacancy concentrations in bcc Ti and W obtained from surface-slab annealing simulations and from vacancy formation free energies. T_{sim} denotes the simulation temperature, while the melting temperature of Ti predicted by MLIP-MD is T_m^{MLIP} =1725±25 K. The quantity $c_V^{MA} = 1 - (n_{atoms}/n_{sites})$ represents the equilibrium concentration of missing atoms in the slab interior (bulk region), primarily originating from vacancies generated at the surface and stabilized in the bulk. Here, n_{atoms} is the number of atoms in the slab interior and n_{sites} is the number of available bulk lattice sites. The smaller and larger surface slabs contain 100800 and 450000 atoms, respectively. The vacancy concentrations c_V^{TI} are obtained from the dilute-limit relation using vacancy formation free energies in **Eq. 4**, **Sec. 4.2**.

Figures

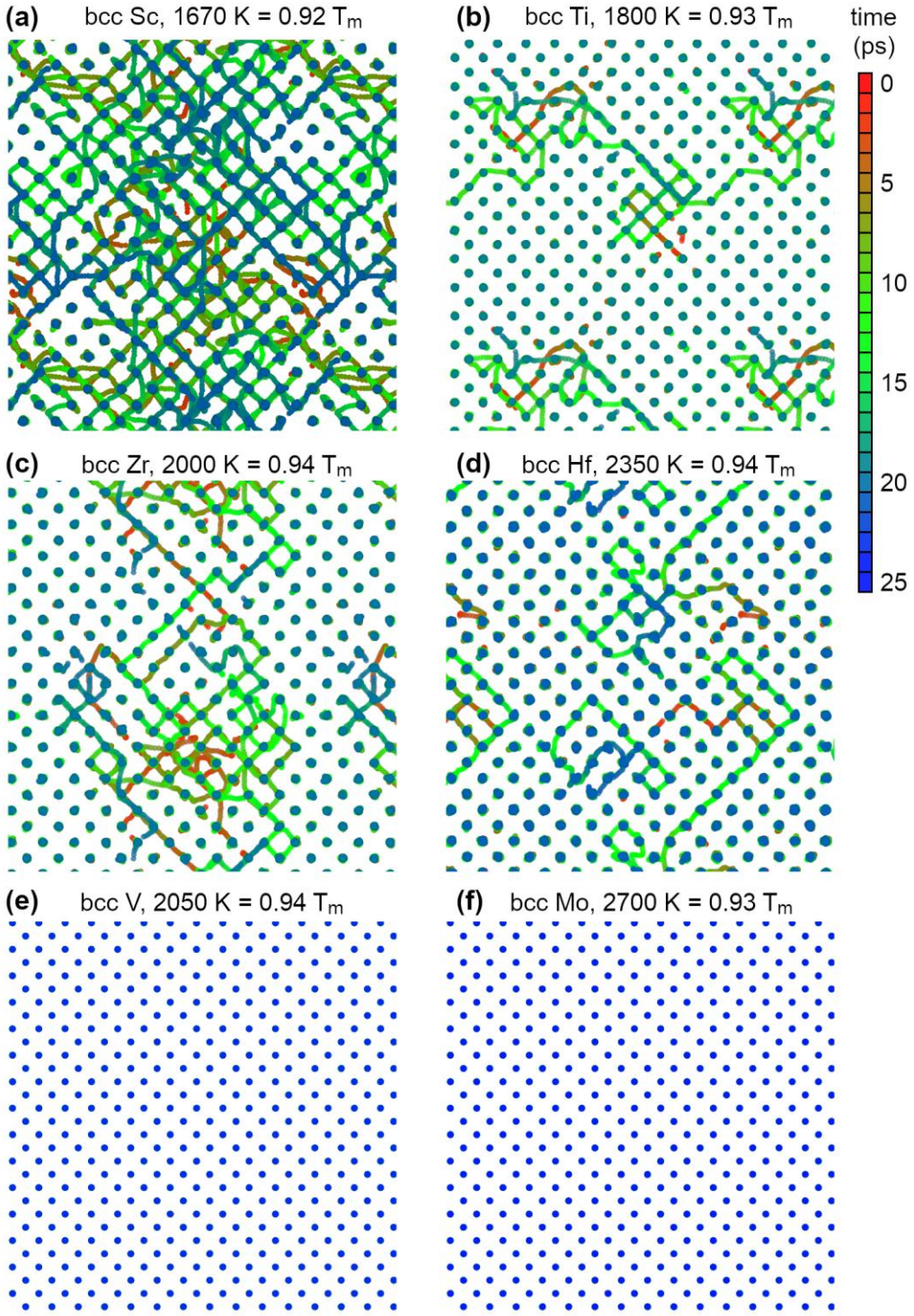


Figure 1. Overlayed AIMD simulation snapshots of bcc metals **(a)** Sc, **(b)** Ti, **(c)** Zr, **(d)** Hf, **(e)** V, and **(f)** Mo near the experimental melting temperatures collected during 25 ps. The coloring of atoms is indicative of time. The snapshots correspond to time-averaged atomic positions, obtained by applying a ±1 ps moving-window average along the AIMD trajectories to smoothen the vibrational noise and clearly distinguish atoms retaining their original position from concerted diffusion reactions. Despite the absence of intrinsic point defects in the supercell, diffusion in Sc, Ti, Zr, and Hf is highly correlated, with strings of atoms concertedly exchanging positions, as indicated by colored horizontal, vertical, and diagonal trajectories. Note that the visible horizontal and vertical trajectories are parallel to ⟨001⟩ crystal axes (orthogonal to the plane of view) while the diagonal motions are inclined to the plane of view and are parallel to ⟨111⟩ crystal axes. By contrast, in bcc V and Mo, all atoms remain at ideal lattice positions during the simulated time. AIMD videos can be found in the **SM** (see **Sec. S6**).

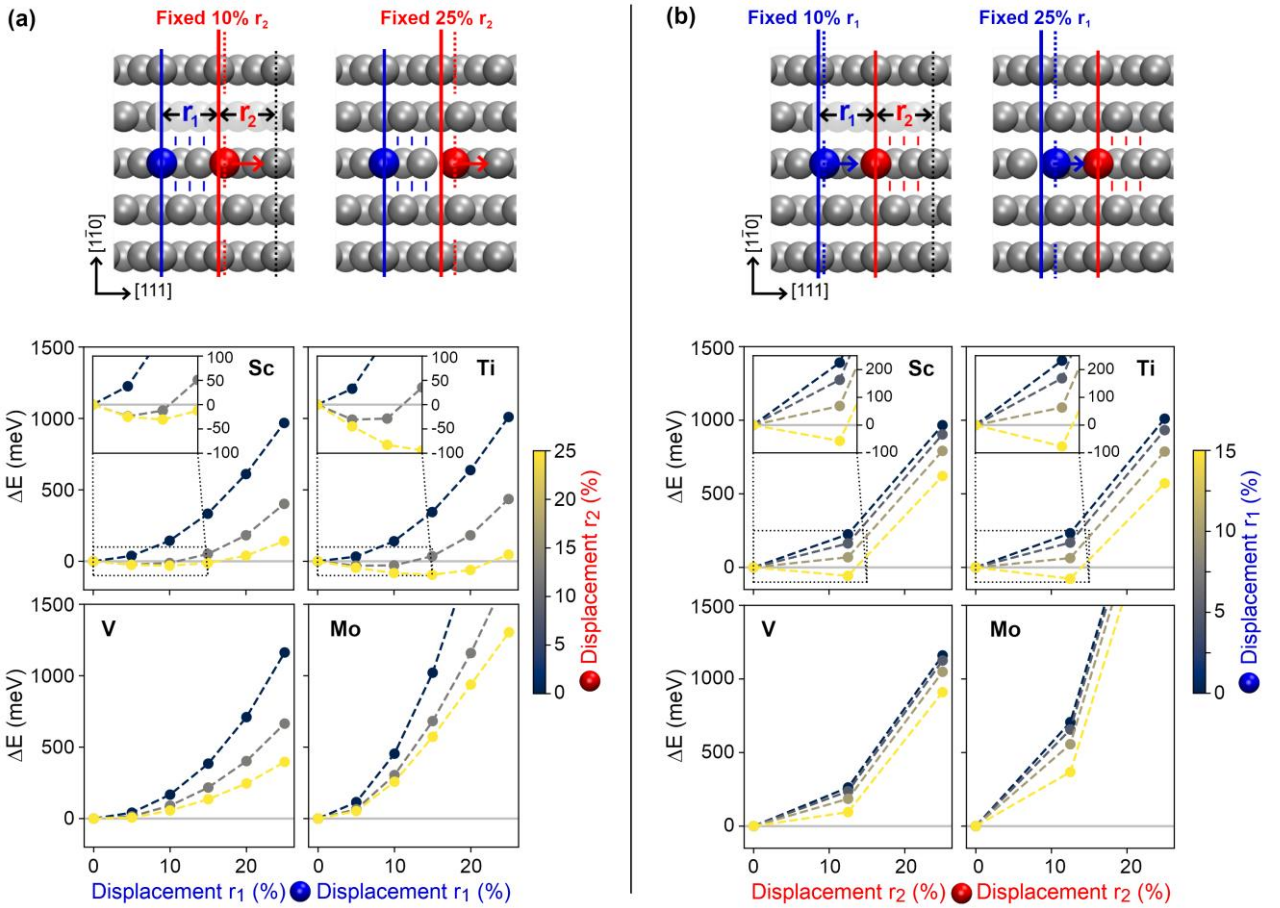


Figure 2. **(a)** Vacancy-like effect on migration energy landscape. DFT energy variations during displacement (r_1) of a lattice atom (atom 1) along the [111] direction while the preceding nearest lattice neighbor (atom 2) is offset by a distance (r_2) from the ideal site along the same [111] direction. The results are collected for bcc Sc, Ti, V, and Mo at their 0-K equilibrium volume. **(b)** Interstitial-like effect on migration energy landscape. DFT energy variations during displacement (r_2) of a lattice atom (atom 2) along the [111] direction while the following nearest lattice neighbor (atom 1) is offset by a distance (r_1) from the ideal site along the same [111] direction. The results are collected for bcc Sc, Ti, V, and Mo at their 0-K equilibrium volume.

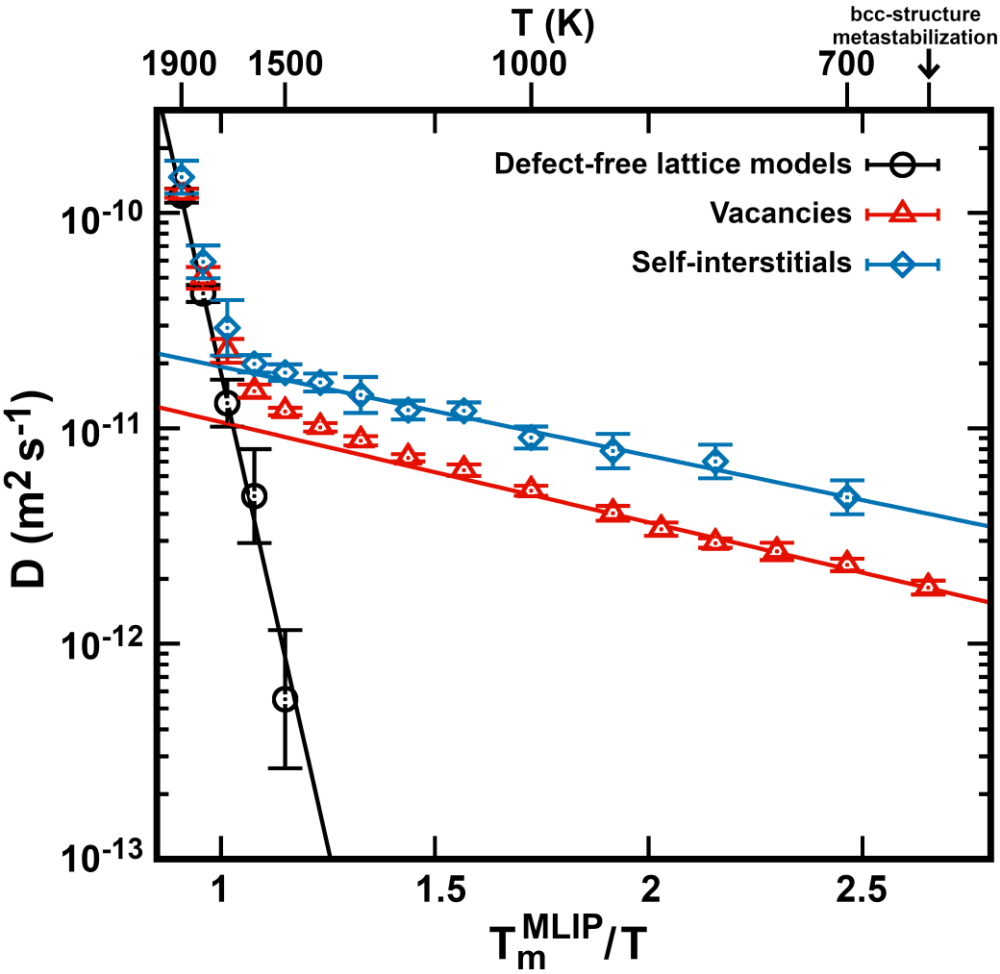


Figure 3. MLIP-MD diffusion coefficients (**Eq. 1**, **Sec. 4.2**) in bcc Ti supercells either initially defect-free (1458 atoms) or containing one vacancy (1457 atoms) or one self-interstitial defect (1459 atoms). The error bars are standard deviations. For temperatures below ~1200 K, the diffusion coefficients of 1457-atom and 1459-atom supercells are well described by linear relations: $D^{V}(T) = \frac{1}{1457}\cdot[(3.0\pm1.3)\cdot10^{-8}\ \mathrm{m^2\ s^{-1}}]\cdot\exp[(-0.13\pm0.03\ \mathrm{eV})/(k_B T)]$ and $D^{SI}(T) = \frac{1}{1459}\cdot[(7.8\pm2.8)\cdot10^{-8}\ \mathrm{m^2\ s^{-1}}\cdot\exp[(-0.14\pm0.03\ \mathrm{eV})/(k_B T)]$. An increase in temperature above 1200 K results in upward bowing in log(D). That is due to diffusion reactions in pristine crystal regions, which provides substantial contribution to mass transport in addition to migration of the native defect. At elevated temperature, the per-atom diffusivity in initially defect-free cells is well approximated by $D^{DF}(T) = (3.5\cdot10^{\pm1})\cdot10^{-3}\ \mathrm{m^2\ s^{-1}}\cdot\exp[(-2.8\pm0.3\ \mathrm{eV})/(k_B T)]$. Note that $T_m^{MLIP} \approx 1725\pm25$ K (see **Fig. S6**).

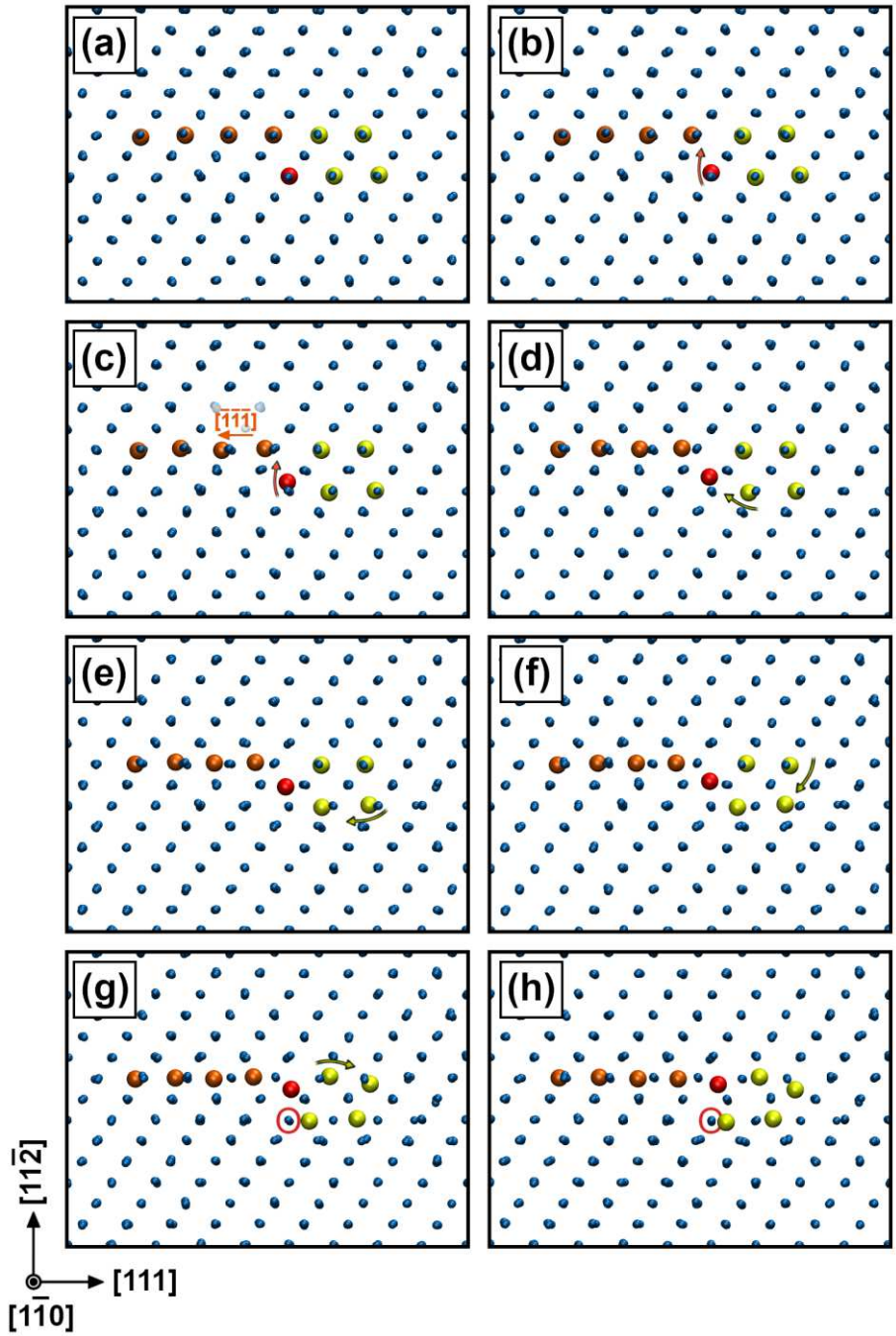


Figure 4. Time-resolved formation and propagation of a vacancy–crowdion-like pair in initially defect-free bcc Ti at 1400 K. Consecutive MLIP-MD snapshots of a 1458-atom supercell are projected onto a {110} plane. Atomic positions are averaged over a 1 ps time window to suppress vibrational noise; successive frames are separated by ~0.3 ps. The sequence illustrates the spontaneous emergence of a Frenkel-like defect configuration. In panels **(a–c)**, a lattice atom (red sphere) leaves its bcc site and moves toward an interstitial position, compressing a ⟨111⟩ lattice row (highlighted in **(c)** by orange spheres and label). The displacement of the red atom exerts a pull on other neighboring atoms (yellow spheres), which subsequently migrate cooperatively **(d-h)** along a four-atom ring toward the vacated site (red empty circle in panels **(g,h)**).

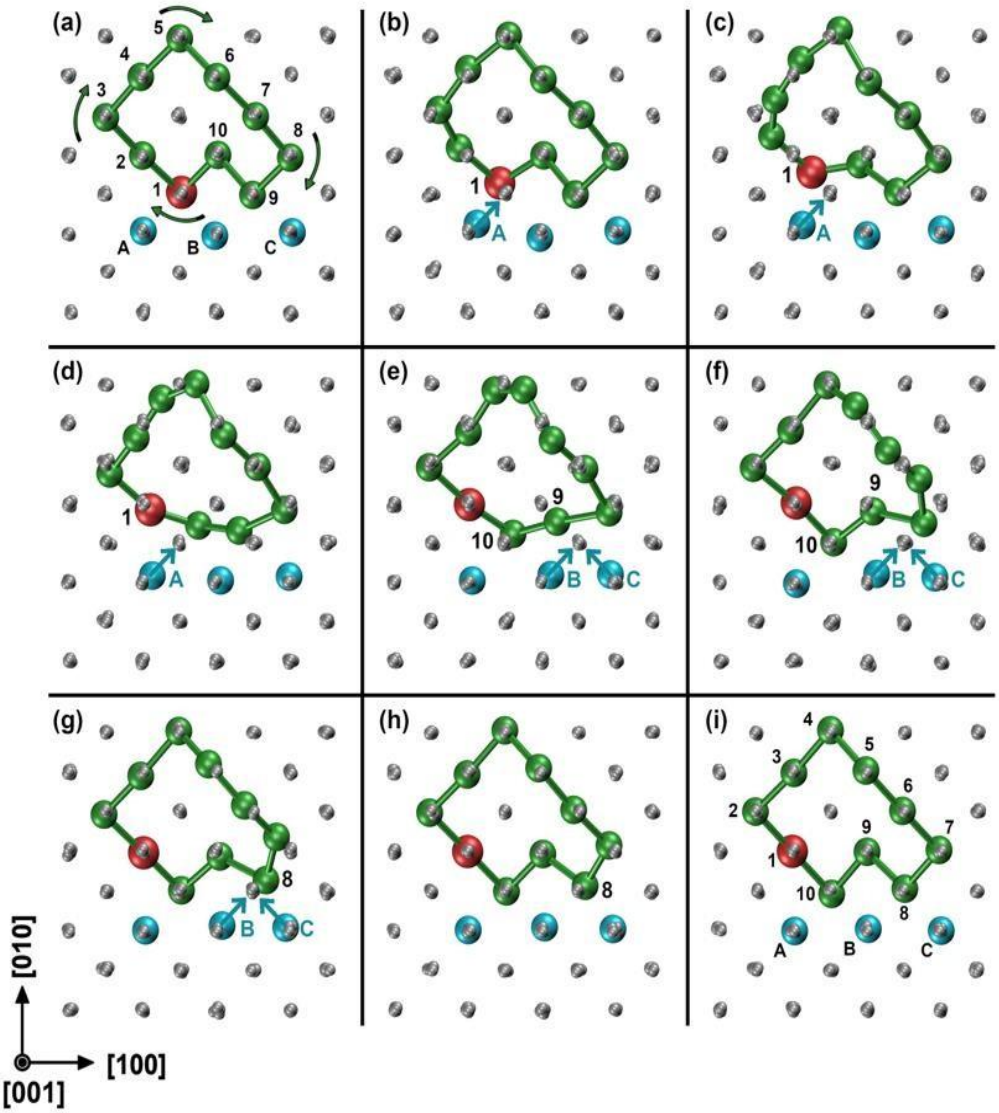


Figure 5. Concerted exchange reactions of a 10-atom ring in bcc Ti at 1400 K. The sequence, projected onto a {001} crystallographic plane, is obtained by MLIP-MD for a 1458-atom supercell initially free of point defects. Atoms of the rotating ring are shown in red (atom 1) and green (atoms 2–9); they are connected by bonds with lengths ≤3.2 Å. Blue atoms indicate neighboring lattice sites that respond to the ring motion; arrows show their instantaneous displacements from ideal bcc positions at times when a neighboring atom has vacated its site, analogous to **Fig. 2a**. Atomic positions are averaged over a 1 ps time window. Each panel corresponds to a time interval of ~0.43 ps, such that the complete ring-rotation event spans about 3.4 ps.

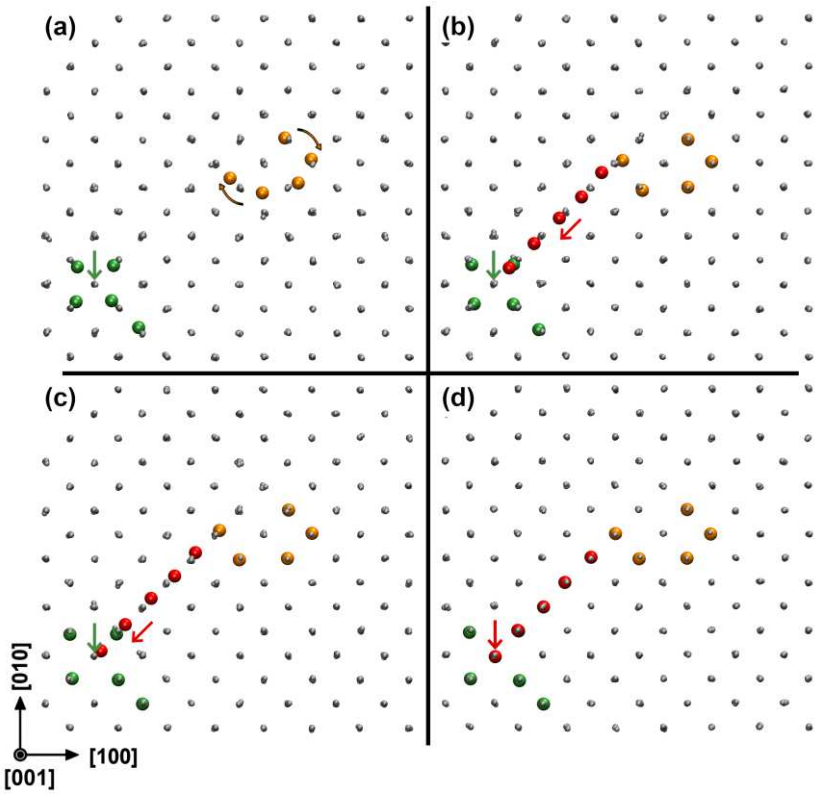


Figure 6. Long-range vacancy–self-interstitial interaction (bridge reaction) in bcc Ti at 1400 K, illustrating a defect-pair annihilation reaction alternative to **Fig. 5**. Snapshots (**a–d**), projected onto a {001} plane, are taken from a 1458-atom MLIP–MD simulation initially free of point defects, with atomic positions averaged over 1 ps. A vacancy-induced lattice distortion (green, arrow) interacts with a five-atom self-interstitial crowdion (orange), triggering a concerted ⟨111⟩ chain translation (red atoms) that links the defects and leads to their recombination within ~3 ps; the vacant site is filled in panel **(d)**.

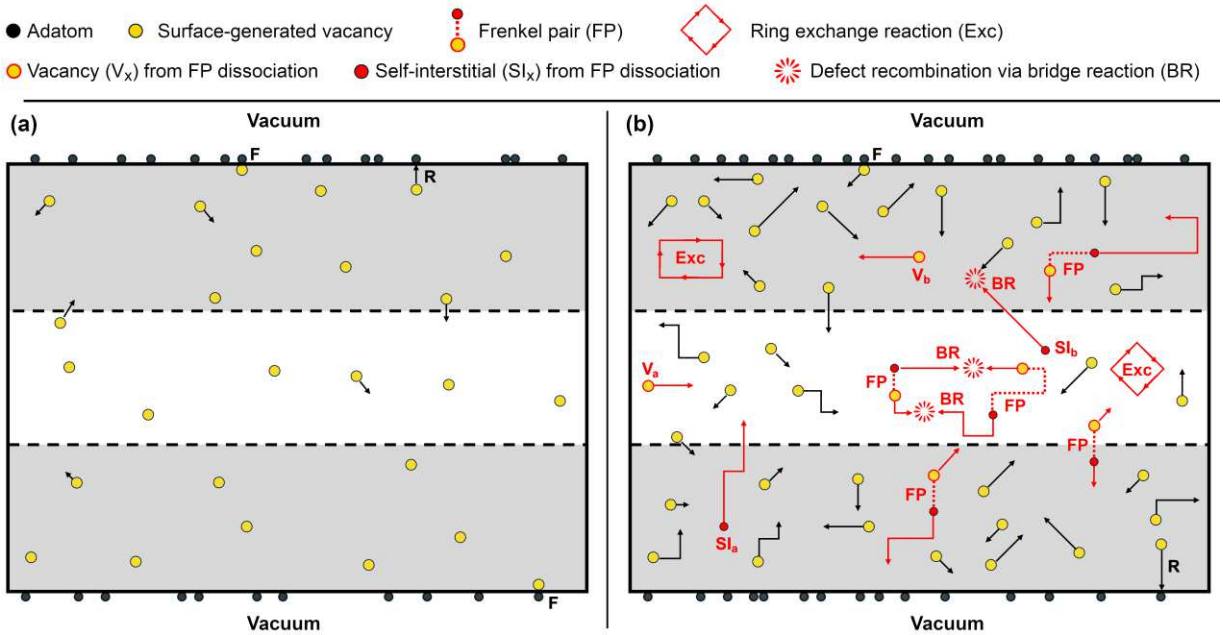


Figure 7. Slab model used to determine equilibrium concentrations of point defects. The white regions represent bulk-like layers that are negligibly affected by surface effects. During equilibration, vacancies form primarily at the surfaces when a surface-layer atom moves outward and becomes an adatom, thereby creating a vacancy–adatom pair [formation (F)]. Vacancies may subsequently diffuse into the interior or recombine (R) with an adatom. Frenkel pairs form directly within the slab interior. The cartoon illustrates two characteristic regimes: **(a)** dilute defect concentration with rare migration events – typical of group-6 metals; **(b)** facile defect formation together with concerted migration of point defects, vacancy–self-interstitial recombination via bridge reactions (as in **Fig. 6**) and ring exchanges – representative of group-4 metals.

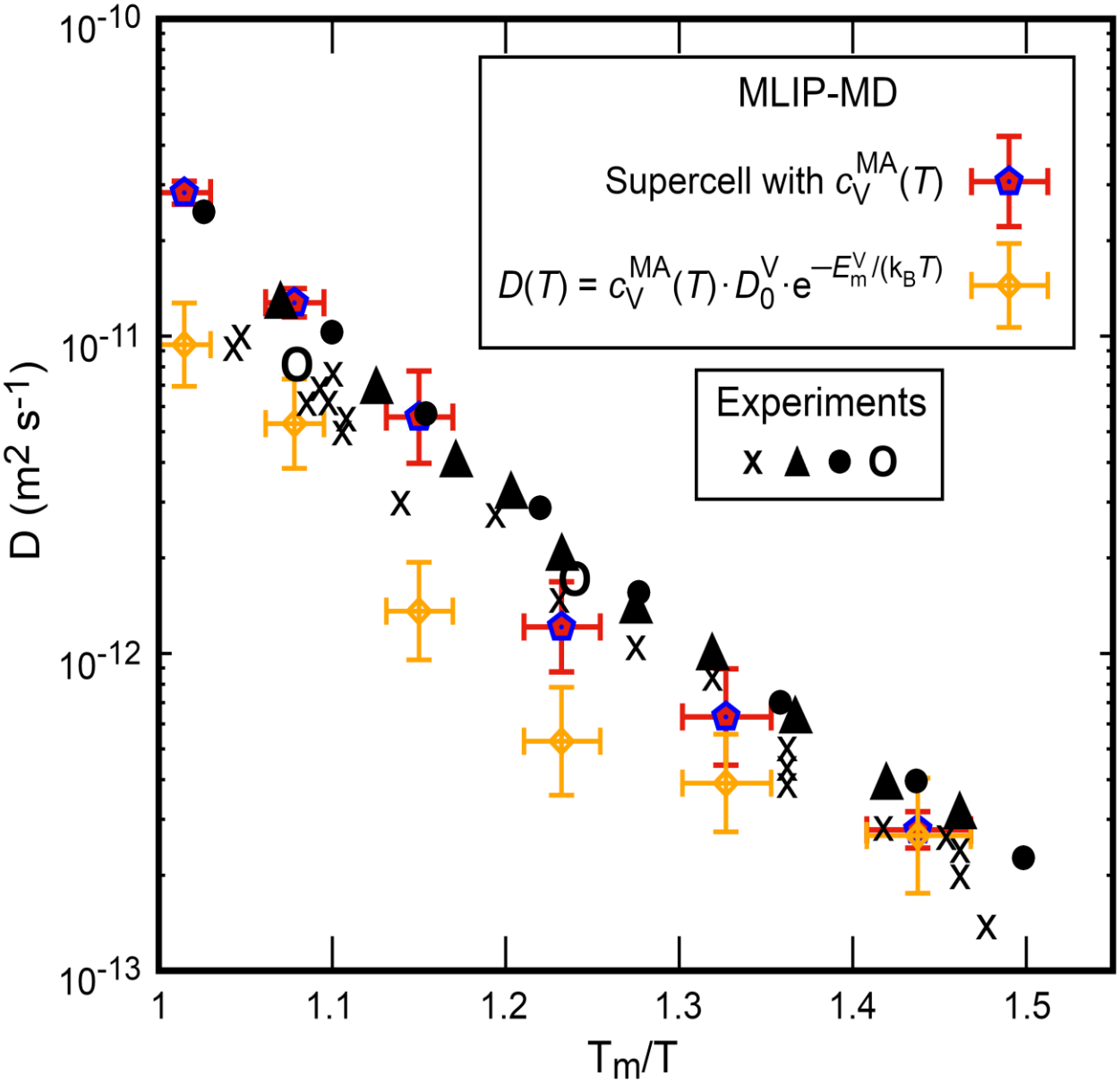


Figure 8. Self-diffusion coefficient of bcc Ti as a function of reduced temperature T_m/T. Experimental data (black symbols) are taken from Refs. [16, 17, 56, 57]. Reduced temperatures used for plotting the experimental data and MLIP-MD simulation results are defined using the experimental melting temperature of Ti (T_m^{expt} =1940 K) and the MLIP-MD melting temperature (T_m^{MLIP} = 1725±25 K; **Fig. S6**), respectively. Red pentagons show direct MLIP-MD results obtained from large supercells containing explicit native vacancies at concentrations chosen to match the independently determined $c_V^{MA}(T)$ values reported in **Table 2**. Orange diamonds correspond to diffusivities estimated as $D(T) = c_V^{MA}(T)\, D_0^V \exp[-E_m^V/(k_B T)]$, where the concentration-independent monovacancy diffusivity parameters (**Eq. 2**, **Sec. 4.2**) are obtained from the low-temperature linear regression in **Fig. 3**, yielding a migration energy E_m^V = 0.13±0.03 eV and a prefactor $D_0^V = (3.0 \pm 1.3) \cdot 10^{-8}$ m² s⁻¹. This Arrhenius relation is linearly extrapolated to temperatures approaching melting.

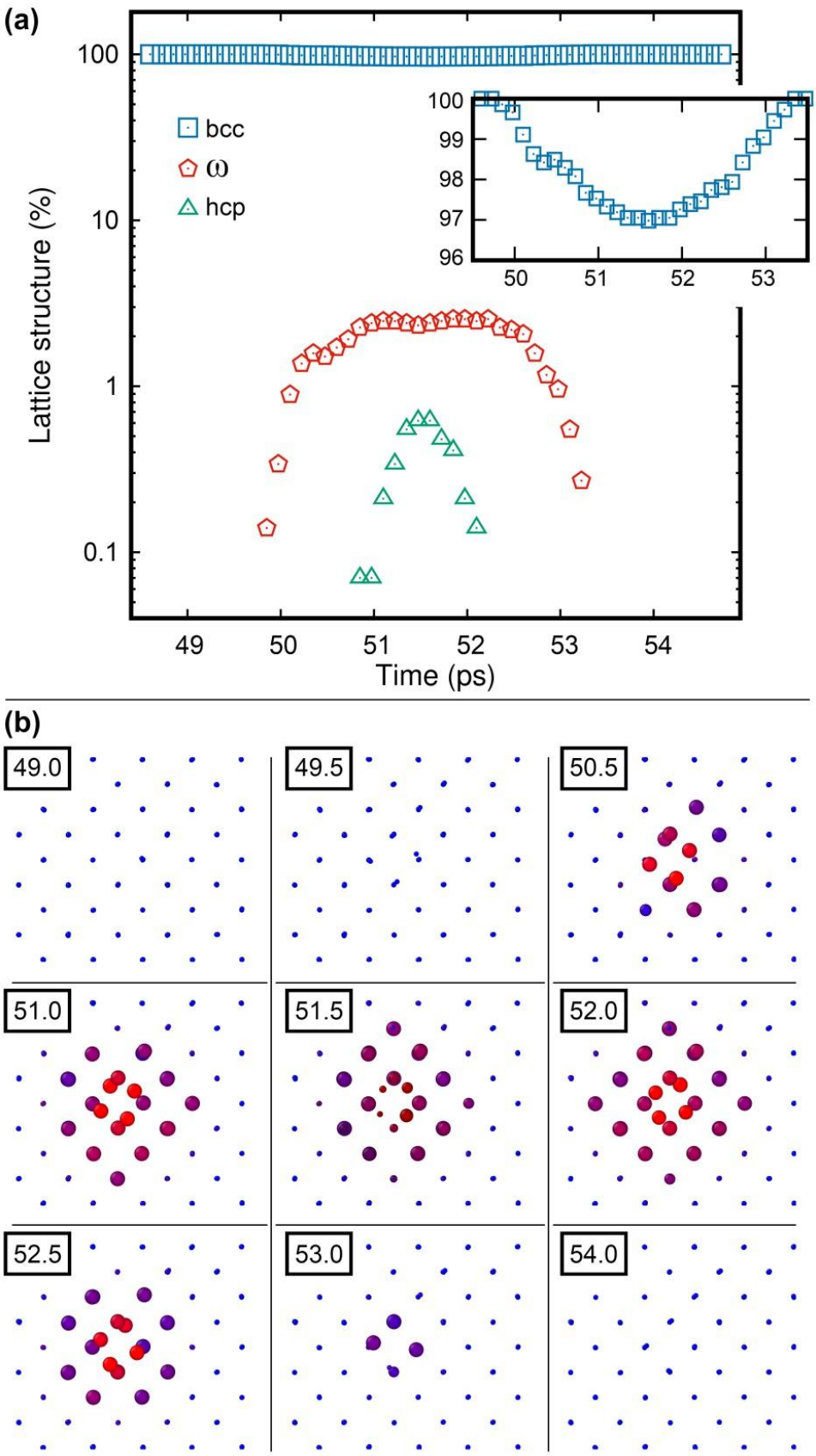


Figure 9. MLIP-MD simulations of defect-free bcc Ti at 1300 K analyzed using Steinhardt structural analysis. **(a)** Average percentage of bcc, ω, and hcp environments encountered along MLIP-MD trajectories. **(b)** MLIP-MD snapshots time-averaged over 1 ps show the formation of ω-like environments associated with a 4-atom ring rotation. The spheres radii ($0.1667 \leq r \leq 0.5$) are given by $r = (p_\omega+0.5)/3$. The rgb colors are computed using the values of the neighbors within a cutoff radius of 3 Å, using the following probabilities: Red – average p_ω; Green – average p_{hcp}; Blue – average p_{bcc}. The fcc and liquid phases (included in the database of the Steinhardt identification of local structures) are never detected during 1 ns.

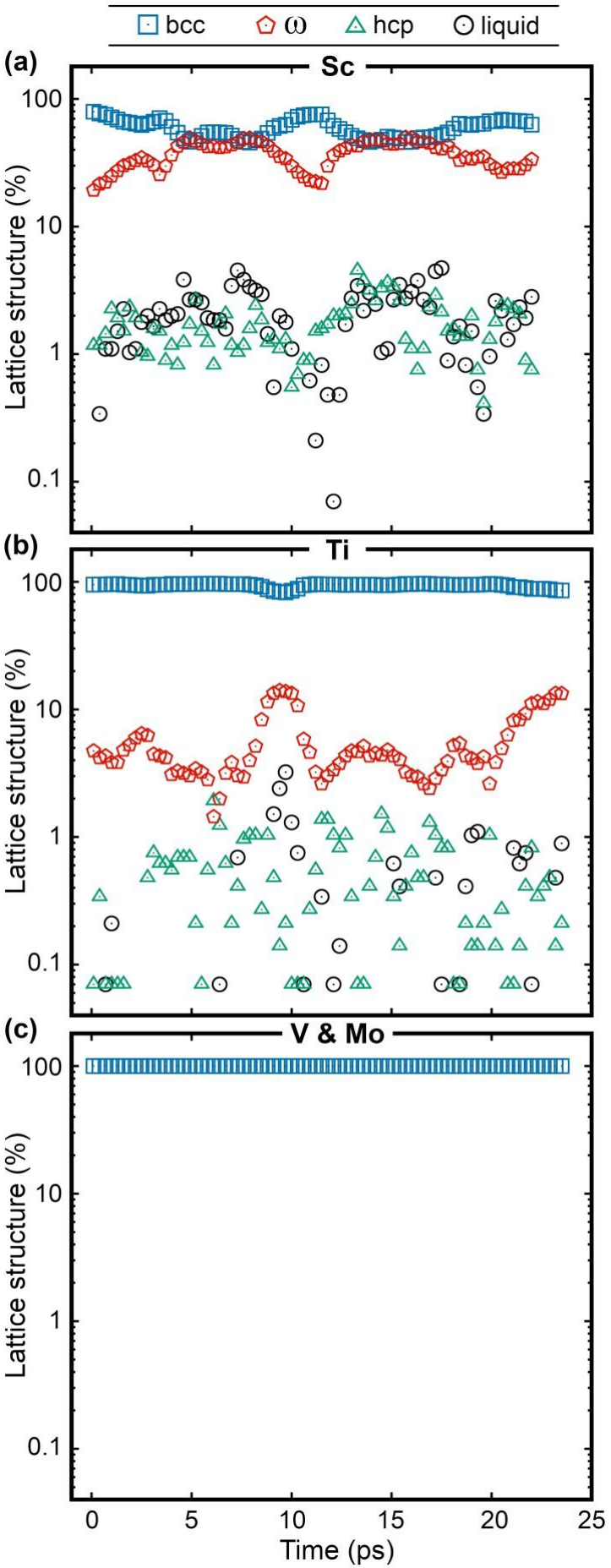


Figure 10. Steinhardt classification of local structural environments encountered during AIMD trajectories (shown in **Fig. 1**) of bcc Sc, Ti, V, and Mo at T_{sim} ~$0.9T_m^{expt}$.

References

[1] P.M. Derlet, D. Nguyen-Manh, S.L. Dudarev, Multiscale modeling of crowdion and vacancy defects in body-centered-cubic transition metals, Physical Review B 76 (2007) 054107.

[2] E. Korznikova, V. Shunaev, I. Shepelev, O. Glukhova, S. Dmitriev, *Ab initio* study of the propagation of a supersonic 2-crowdion in fcc Al, Computational Materials Science 204 (2022) 111125.

[3] Y. Matsukawa, S. Zinkle, One-dimensional fast migration of vacancy clusters in metals, Science 318 (2007) 959.

[4] B. van der Meer, R. van Damme, M. Dijkstra, F. Smallenburg, L. Filion, Revealing a Vacancy Analog of the Crowdion Interstitial in Simple Cubic Crystals, Physical Review Letters 121 (2018) 258001.

[5] H.B. Huntington, F. Seitz, Mechanism for self-diffusion in metallic copper, Physical Review 61 (1942) 315.

[6] C. Zener, Ring diffusion in metals, Acta Crystallographica 3 (1950) 346.

[7] K. Pandey, Diffusion without vacancies or interstitials – a new concerted exchange mechanism, Physical Review Letters 57 (1986) 2287.

[8] A.B. Belonoshko, T. Lukinov, J. Fu, J. Zhao, S. Davis, S.I. Simak, Stabilization of body-centred cubic iron under inner-core conditions, Nature Geoscience 10 (2017) 312.

[9] M. Ghosh, S. Zhang, L. Hu, S.X. Hu, Cooperative diffusion in body-centered cubic iron in Earth and super-Earths' inner core conditions, Journal of Physics: Condensed Matter 35 (2023) 154002.

[10] Y. Zhang, Y. Wang, Y. Huang, J. Wang, Z. Liang, L. Hao, Z. Gao, J. Li, Q. Wu, H. Zhang, Y. Liu, J. Sun, J. Lin, Collective motion in hcp-Fe at Earth's inner core conditions, PNAS 120 (2023) e2309952120.

[11] Y. Wang, J. Wang, A. Hermann, C. Liu, H. Gao, E. Tosatti, H.-T. Wang, D. Xing, J. Sun, Electronically driven 1d cooperative diffusion in a simple cubic crystal, Physical Review X 11 (2021) 011006.

[12] Y. Wang, J. Wang, A. Hermann, S. Pan, J. Shi, H.-T. Wang, D. Xing, J. Sun, Temperature-induced electride transition in dense lithium, Physical Review B 105 (2022) 214101.

[13] V. Robinson, H. Zong, G. Ackland, G. Woolman, A. Hermann, On the chain-melted phase of matter, PNAS 116 (2019) 10297.

[14] F. Willaime, C. Massobrio, A molecular dynamics study of zirconium based on an N-body potential: hcp/bcc phase transformation and diffusion mechanisms in the bcc phase, MRS Online Proceedings Library 193 (1990) 295.

[15] D.G. Sangiovanni, J. Klarbring, D. Smirnova, N.V. Skripnyak, D. Gambino, M. Mrovec, S.I. Simak, I.A. Abrikosov, Superioniclike Diffusion in an Elemental Crystal: bcc Titanium, Physical Review Letters 123 (2019) 105501.

[16] A.E. Pontau, D. Lazarus, Diffusion of titanium and niobium in bcc Ti-Nb alloys, Physical Review B 19 (1979) 4027.

[17] U. Köhler, C. Herzig, On the anomalous self-diffusion in bcc titanium, Physica Status Solidi B 144 (1987) 243.

[18] E. Fransson, P. Erhart, Defects from phonons: Atomic transport by concerted motion in simple crystalline metals, Acta Materialia 196 (2020) 770.

[19] J.H. Jung, A. Forslund, P. Srinivasan, B. Grabowski, Dynamically stabilized phases with full *ab initio* accuracy: Thermodynamics of Ti, Zr, Hf with a focus on the hcp-bcc transition, Physical Review B 108 (2023) 184107.

[20] J. Zhang, J. Douglas, H. Zhang, String-like collective motion mediates the martensitic α-β transition in titanium, Journal of Chemical Physics 163 (2025) 044504.
[21] X. Fan, D. Pan, M. Li, Melting of bcc crystal Ta without the Lindemann criterion, Journal of Physics: Condensed Matter 31 (2019) 095402.
[22] C. Wu, P. Söderlind, J. Glosli, J. Klepeis, Shear-induced anisotropic plastic flow from body-centred-cubic tantalum before melting, Nature Materials 8 (2009) 223.
[23] G. Zhang, X. Fan, Q. Zhang, Q. Li, Y. Wu, M. Li, Partial disordering and homogeneous melting in multicomponent systems, Acta Materialia 239 (2022) 118281.
[24] G. Smirnov, Non-Arrhenius diffusion in bcc titanium: Vacancy-interstitialcy model, Physical Review B 102 (2020) 184110.
[25] X. Zhang, S. Divinski, B. Grabowski, Ab initio machine-learning unveils strong anharmonicity in non-Arrhenius self-diffusion of tungsten, Nature Communications 16 (2025) 394.
[26] D.E. Smirnova, S.V. Starikov, I.S. Gordeev, Evaluation of the structure and properties for the high-temperature phase of zirconium from the atomistic simulations, Computational Materials Science 152 (2018) 51.
[27] D. Smirnova, S. Starikov, G.D. Leines, Y. Liang, N. Wang, M.N. Popov, I.A. Abrikosov, D.G. Sangiovanni, R. Drautz, M. Mrovec, Atomistic description of self-diffusion in molybdenum: A comparative theoretical study of non-Arrhenius behavior, Physical Review Materials 4 (2020) 013610.
[28] T.R. Mattsson, N. Sandberg, R. Armiento, A.E. Mattsson, Quantifying the anomalous self-diffusion in molybdenum with first-principles simulations, Physical Review B 80 (2009) 224104.
[29] D.G. Sangiovanni, O. Hellman, B. B. Alling, I.A. Abrikosov, Efficient and accurate determination of lattice-vacancy diffusion coefficients via nonequilibrium *ab initio* molecular dynamics, Physical Review B 93 (2016) 094305.
[30] L. Zepeda-Ruiz, J. Rottler, S. Han, G. Ackland, R. Car, D. Srolovitz, Strongly non-Arrhenius self-interstitial diffusion in vanadium, Physical Review B 70 (2004) 060102.
[31] S. Kadkhodaei, A. Davariashtiyani, Phonon-assisted diffusion in bcc phase of titanium and zirconium from first principles, Physical Review Materials 4 (2020) 043802.
[32] S. Fattahpour, A. Davariashtiyani, S. Kadkhodaei, Understanding the role of anharmonic phonons in diffusion of bcc metals, Physical Review Materials 6 (2022) 023803.
[33] C. Lapointe, A. Zhong, T. Swinburne, F. Bruneval, M. Marinica, Anomalous self-diffusion in tungsten and molybdenum: Exonerating the di-vacancy contribution and the key role of interatomic interaction, Physical Review Materials 9 (2025) 093601.
[34] J.M. Sanchez, D.D. Fontaine, Model for anomalous self-diffusion in group-IVB transition metals, Physical Review Letters 35 (1975) 227.
[35] U. Kohler, C. Herzig, On the correlation between self-diffusion and the low-frequency LA 2/3(111) phonon mode in bcc metals, Philosophical Magazine A 58 (1988) 769.
[36] J. Trampenau, W. Petry, A. Heiming, Phonons in the bcc phase of Sc, Physica B 180 (1992) 363.
[37] D. Djurovic, M. Zinkevich, F. Aldinger, Thermodynamic modeling of the yttrium-oxygen system, CALPHAD 31 (2007) 560.
[38] M. Tenhover, B. Clemens, P. Duwez, A body-centered cubic phase of elemental yttrium prepared by the rapid solidification of yttrium iron alloys, Journal of Physics F: Metal Physics 12 (1982) L167.

[39] F. Guthoff, W. Petry, C. Stassis, A. Heiming, B. Hennion, C. Herzig, Phonon dispersion of bcc La, Physical Review B 47 (1993) 2563.
[40] P. Souvatzis, T. Björkman, O. Eriksson, P. Andersson, M. Katsnelson, S. Rudin, Dynamical stabilization of the body centered cubic phase in lanthanum and thorium by phonon-phonon interaction, Journal of Physics: Condensed Matter 21 (2009) 175402.
[41] F.H. Spedding, J.J. Hanak, A.H. Daane, High temperature allotropy and thermal expansion of the rare-earth metals, Journal of the Less Common Metals 3 (1961) 110.
[42] W. Petry, A. Heiming, J. Trampenau, M. Alba, C. Herzig, H.R. Schober, G. Vogl, Phonon dispersion of the bcc phase of group-IV metals. I. Bcc titanium, Physical Review B 43 (1991) 10933.
[43] A. Heiming, W. Petry, J. Trampenau, M. Alba, C. Herzig, H.R. Schober, G. Vogl, Phonon dispersion of the bcc phase of group-IV metals. II. Bcc zirconium, Physical Review B 43 (1991) 10948.
[44] J. Trampenau, A. Heiming, W. Petry, M. Alba, C. Herzig, W. Miekeley, H.R. Schober, Phonon dispersion of the bcc phase of group-IV metals. III. Bcc hafnium, Physical Review B 43 (1991) 10963.
[45] J. Robertson, H. Frase, P. Bogdanoff, M. Manley, B. Fultz, R. McQueeney, Phonon densities of states of γ-cerium and δ-cerium measured by inelastic neutron scattering, Philosophical Magazine Letters 79 (1999) 297.
[46] K. Nicolaus, J. Neuhaus, W. Petry, J. Bossy, Phonon dispersion of bcc cerium, European Physical Journal B 21 (2001) 357.
[47] K. Persson, M. Ekman, V. Ozolins, Phonon instabilities in bcc Sc, Ti, La, and Hf, Physical Review B 61 (2000) 11221.
[48] Z.-G. Mei, S.-L. Shang, Y. Wang, Z.-K. Liu, Density-functional study of the thermodynamic properties and the pressure–temperature phase diagram of Ti, Physical Review B 80 (2009) 104116.
[49] G. Grad, P. Blaha, J. Luitz, K. Schwarz, A. Guillermet, S. Sferco, Electronic structure and chemical bonding effects upon the bcc–ω phase transition: ab initio study of Y, Zr, Nb, and Mo, Physical Review B 62 (2000) 12743.
[50] P. Souvatzis, O. Eriksson, M. Katsnelson, S. Rudin, Entropy driven stabilization of energetically unstable crystal structures explained from first principles theory, Physical Review Letters 100 (2008) 095901.
[51] E.I. Isaev, S.I. Simak, I.A. Abrikosov, R. Ahuja, Y.K. Vekilov, M.I. Katsnelson, A.I. Lichtenstein, B. Johansson, Phonon related properties of transition metals, their carbides, and nitrides: a first-principles study, Journal of Applied Physics 101 (2007) 123519.
[52] L. Zhu, P. Srinivasan, Y. Gong, T. Hickel, B. Grabowski, F. Körmann, J. Neugebauer, Melting properties of the refractory metals V and W and the binary VW alloy fully from first principles, Physical Review B 109 (2024) 094110.
[53] L.-F. Zhu, B. Grabowski, J. Neugebauer, Efficient approach to compute melting properties fully from *ab initio* with application to Cu, Physical Review B 96 (2017) 224202.
[54] L. Zhu, F. Körmann, A. Ruban, J. Neugebauer, B. Grabowski, Performance of the standard exchange-correlation functionals in predicting melting properties fully from first principles: application to Al and magnetic Ni, Physical Review B 101 (2020) 144108.
[55] G. Vogl, W. Petry, T. Flottmann, A. Heiming, Direct determination of the self-diffusion mechanism in bcc β-titanium, Physical Review B 39 (1989) 5025.

[56] J.F. Murdock, T.S. Lundy, E.E. Stansbury, Diffusion of Ti^{44} and V^{48} in titanium, Acta Metallurgica 12 (1964) 1033.
[57] N.E. Walsöe de Reca, C.M. Libanati, Self diffusion in β-titanium and β-hafnium, Acta Metallurgica 16 (1968) 1297.
[58] C. Herzig, U. Köhler, The influence of scandium on the anomalous self-diffusion in bcc zirconium, Acta Metallurgica 35 (1987) 1831.
[59] G. Kidson, J. McGurn, Self-diffusion in body-centered cubic zirconium, Canadian Journal of Physics 39 (1961) 1146.
[60] W. Petry, A. Heiming, C. Herzig, J. Trampenau, On the diffusion mechanism in bcc metals: a neutron scattering approach, Trans Tech Publications 75 (1991) 211.
[61] W. Petry, A. Heiming, J. Trampenau, M. Alba, G. Vogl, Strong phonon softening in the bcc phase of titanium, Physica B 156 (1989) 56.
[62] W. Petry, Phonons at martensitic phase transitions of bcc-Ti, bcc-Zr and bcc-Hf, Phase Transitions 31 (1991) 119.
[63] K.M. Ho, C.L. Fu, B.N. Harmon, Vibrational frequencies via total-energy calculations: applications to transition metals, Physical Review B 29 (1984) 1575.
[64] S.L. Shang, L.G. Hector, Y. Wang, Z.K. Liu, Anomalous energy pathway of vacancy migration and self-diffusion in hcp Ti, Physical Review B 83 (2011) 224104.
[65] F. Dyment, C.M. Libanati, Self-diffusion of Ti, Zr, and Hf in their hcp phases and diffusion of Nb^{95} in hcp Zr, Journal of Materials Science 3 (1968) 349.
[66] B. Zhang, Z. Zhang, K. Xun, M. Asta, J. Ding, E. Ma, Minimizing the diffusivity difference between vacancies and interstitials in multi-principal element alloys, PNAS 121 (2024) e2314248121.
[67] S. Dudarev, The non-Arrhenius migration of interstitial defects in bcc transition metals, Comptes Rendus Physique 9 (2008) 409.
[68] D.G. Sangiovanni, B. Alling, P. Steneteg, L. Hultman, I.A. Abrikosov, Nitrogen vacancy, self-interstitial diffusion, and Frenkel-pair formation/dissociation in B1 TiN studied by *ab initio* and classical molecular dynamics with optimized potentials, Physical Review B 91 (2015) 054301.
[69] D. Korbmacher, A. Glensk, A.I. Duff, M.W. Finnis, B. Grabowski, J. Neugebauer, *Ab initio* based method to study structural phase transitions in dynamically unstable crystals, with new insights on the β to ω transformation in titanium, Physical Review B 100 (2019) 104110.
[70] W.-S. Ko, B. Grabowski, J. Neugebauer, Development and application of a Ni-Ti interatomic potential with high predictive accuracy of the martensitic phase transition, Physical Review B 92 (2015) 134107.
[71] S. Gelin, A. Champagne-Ruel, N. Mousseau, Enthalpy-entropy compensation of atomic diffusion originates from softening of low frequency phonons, Nature Communications 11 (2020) 3977.
[72] G.H. Vineyard, Frequency factors and isotope effects in solid state rate processes, Journal of Physics and Chemistry of Solids 3 (1957) 121.
[73] A. Glensk, B. Grabowski, T. Hickel, J. Neugebauer, Breakdown of the Arrhenius law in describing vacancy formation energies: the importance of local anharmonicity revealed by *ab initio* thermodynamics, Physical Review X 4 (2014) 011018.
[74] H. Wang, Y. Wu, Direct monitoring of vacancy thermal equilibration, Journal of Physical Chemistry Letters 16 (2025) 6608.
[75] G. Kresse, J. Furthmüller, Efficient iterative schemes for *ab initio* total-energy calculations using a plane-wave basis set, Physical Review B 54 (1996) 11169.

[76] G. Kresse, D. Joubert, From ultrasoft pseudopotentials to the projector augmented-wave method, Physical Review B 59 (1999) 1758.
[77] J.P. Perdew, K. Burke, M. Ernzerhof, Generalized gradient approximation made simple, Physical Review Letters 77 (1996) 3865.
[78] F. Grasselli, Investigating finite-size effects in molecular dynamics simulations of ion diffusion, heat transport, and thermal motion in superionic materials, Journal of Chemical Physics 156 (2022) 134705.
[79] A.V. Shapeev, Moment tensor potentials: a class of systematically improvable interatomic potentials, Multiscale Modeling & Simulation 14 (2016) 1153.
[80] A.P. Thompson, H.M. Aktulga, R. Berger, D.S. Bolintineanu, W.M. Brown, P.S. Crozier, P.J. in 't Veld, A. Kohlmeyer, S.G. Moore, T.D. Nguyen, R. Shan, M.J. Stevens, J. Tranchida, C. Trott, S.J. Plimpton, LAMMPS: a flexible simulation tool for particle-based materials modeling at the atomic, meso, and continuum scales, Computer Physics Communications 271 (2022) 108171.
[81] S. Starikov, P. Grigorev, R. Drautz, S. Divinski, Large-scale atomistic simulation of diffusion in refractory metals and alloys, Physical Review Materials 8 (2024) 043601.
[82] M.I. Mendelev, Y. Mishin, Molecular dynamics study of self-diffusion in bcc Fe, Physical Review B 80 (2009) 144111.
[83] W. Humphrey, A. Dalke, K. Schulten, VMD: visual molecular dynamics, Journal of Molecular Graphics and Modelling 14 (1996) 33.
[84] A. Stukowski, Visualization and analysis of atomistic simulation data with OVITO – the open visualization tool, Modelling and Simulation in Materials Science and Engineering 18 (2010) 015012.
[85] D. Kammler, M. Rodriguez, R. Tissot, D. Brown, B. Clausen, T. Sisneros, In-situ time-of-flight neutron diffraction study of high-temperature α-to-β phase transition in elemental scandium, Metallurgical and Materials Transactions A 39 (2008) 2815.
[86] O. Senkov, B. Chakoumakos, J. Jonas, F. Froes, Effect of temperature and hydrogen concentration on the lattice parameter of β-titanium, Materials Research Bulletin 36 (2001) 1431.
[87] A. Heiming, W. Petry, J. Trampenau, W. Miekeley, J. Cockcroft, The temperature dependence of the lattice parameters of pure bcc Zr and bcc Zr-2 at.% Co, Journal of Physics: Condensed Matter 4 (1992) 727.
[88] R.G. Ross, W. Hume-Rothery, High temperature X-ray metallography, Journal of the Less Common Metals 5 (1963) 258.
[89] K. Wang, R.R. Reeber, The role of defects on thermophysical properties: thermal expansion of V, Nb, Ta, Mo and W, Materials Science and Engineering R 23 (1998) 101.

Supplementary Files

This is a list of supplementary files associated with this preprint. Click to download.

- Supplementalmaterial.pdf
- Video1bccSc.mp4
- Video2bccTi.mp4
- Video3bccZr.mp4
- Video4bccHf.mp4
- Video5bccV.mp4